S-coda and Rayleigh waves from a decade of repeating earthquakes reveal discordant temporal velocity changes since the 2004 Sumatra Earthquake

W. Yu[1], J.-T. Lin[2], J. Su[1], T.-R. A. Song[3], and C.-C. Kang[4]

[1] Institute of Earth Sciences, Academia Sinica, No. 128, Section 2, Academia Road, Nangang, Taipei, 11529, Taiwan, Republic of China

[2] Department of Earth Sciences, University of Oregon, Earth Sciences Department, 100 Cascade Hall, 1272 University of Oregon, Eugene, OR 97403, United States of America

[3] Department of Earth Sciences, University College London, Gower Street, London, WC1E 6BT, United Kingdom

[4] Department of Natural Sciences and Sustainable Development, Ministry of Science and Technology, No. 106, Section 2, Heping East Road, Taipei, 10622, Taiwan, Republic of China

Corresponding author: W. Yu (fgsyw@earth.sinica.edu.tw)

Submitted to *Journal of Geophysical Research*: *Solid Earth*

Formatted

Key Points

- High-frequency *S*-coda and long-period Rayleigh waves from repeating earthquakes reveal velocity changes since the 2004 Sumatra Earthquake
- *S*-coda velocity changes underwent steady recovery from 2005 to 2015, while Rayleigh wave velocities decreased significantly in late 2007
- Temporal differences in *S*-coda and Rayleigh velocity changes can delineate slow deformation at depth and healing of the surface damage zone

Abstract

Temporal changes in the subsurface seismic velocity structure reflect the physical processes that modulate the properties of the media through which seismic waves propagate. These processes, such as healing of the surface damage zone and deep crustal deformation, are described by similar functions and operate on similar timescales, making it difficult to determine which process drives the observed changes. We examine earthquake-induced velocity changes using the measured lag-time time series $\tau(t)$ of the repeating earthquake sequences since the 2004 M_w 9.2 Sumatra and 2005 M_w 8.6 Nias earthquakes. The *S*-coda velocity changes (δV_S, equivalent to $-\tau_S$) recover steadily during the 2005−2015 period. The Rayleigh wave velocity changes (δV_{LR}, or $-\tau_{LR}$) undergo transient recovery, followed by a strong δV_{LR} reduction in late 2007. δV_S recovery is most likely driven by deep processes, whereas the temporal breaks in δV_{LR} recovery in 2007 reflect surface damage and healing induced by the strong ground motions of the 2004 M_w 9.2, 2005 M_w 8.6, 2007 M_w 8.4 and M_w 7.9 Bengkulu, and 2008 M_w 7.3 Simeulue earthquakes. The observed differences between the temporal variations in δV_S and δV_{LR} can distinguish deep processes from healing of the surface damage zone.

41

42 **Plain language summary**

43 Earthquake slip leads to stress relaxation in the crust, whereas healing of the damage induced
44 by strong ground motion predominantly occurs in the near-surface. Temporal changes in the seismic
45 velocity structure after large earthquakes can be driven by diverse mechanisms, such as aseismic slip
46 or fault zone healing, but the timescales governing these processes are very similar, making them
47 difficult to distinguish. We detect temporal velocity changes in the crust since the great 2004 Sumatra
48 and 2005 Nias earthquakes using the high-frequency late-arriving scattered waves after the *S* phase
49 and long-period Rayleigh waves of repeating earthquakes. We find that the temporal velocity changes
50 in the scattered waves exhibit steady logarithmic recovery from 2005 to 2015, whereas the Rayleigh-
51 wave velocity recovery was interrupted by several large earthquakes after late 2007. The difference
52 between these two temporal trends in velocity change is the key to distinguishing between a
53 damage/healing/re-damage cycle near the surface and slow deformation (e.g., afterslip, post-seismic
54 relaxation) at depth. Rayleigh waves are highly sensitive to the near-surface damage and healing after
55 the 2004/2005 events, and also the repeated damage induced by the 2007 and 2008 earthquakes.
56 Steady velocity recovery of the scattered waves primarily corresponds to slow deformation at depth.

57

58 **1. Introduction**

59 Long-term monitoring of temporal seismic-velocity variations in the crust is an important and
60 long-sought goal in geophysics because these temporal changes can be proxy measures for the
61 mechanical processes and timescales of crustal responses to earthquake slip. Numerous studies have
62 suggested that these temporal velocity changes are often associated with the peak ground velocity
63 (PGV) or acceleration (PGA) that is induced by the strong ground motion (GM) of an earthquake
64 [*Rubinstein and Beroza*, 2004a; *Schaff and Beroza*, 2004; *Y. G. Li et al.*, 2006; *Rubinstein et al.*, 2007;

Wegler et al., 2009; *Takagi et al.*, 2012; *T. Yu and Hung*, 2012; *Hobiger et al.*, 2016]. Strong GM damages the subsurface sediment layer, which is subjected to low confining pressures of only a few tens of MPa [*Wu et al.*, 2009; *Zhao and Peng*, 2009; *Sawazaki et al.*, 2015; *L. Li et al.*, 2017]. The subsequent velocity recovery, which probably reflects healing of the subsurface damage zone, is typically characterized by a logarithmic time dependence (so-called "slow dynamics") [*TenCate et al.*, 2000; *Peng and Ben-Zion*, 2006; *Brenguier et al.*, 2008; *Snieder et al.*, 2017].

These temporal velocity changes may also be associated with aseismic slip (or slip rate), post-seismic afterslip [*Rivet et al.*, 2011; *W. Yu et al.*, 2013a], and viscoelastic relaxation in the bulk crust. Post-seismic transients due to afterslip and dilatancy recovery occur adjacent to the earthquake slip zone, and can modulate the crack density and pore pressure, yielding recoveries in *S*-wave velocity and Poisson's ratio [*Peltzer et al.*, 1996; *Fialko*, 2004; *Fielding et al.*, 2009]. Viscoelastic relaxation mainly occurs in the lower crust and upper mantle over longer timescales, and can restore the stress perturbation induced by co-seismic slip [*Barbot and Fialko*, 2010; *Qiu et al.*, 2018; *Tang et al.*, 2019]. Post-seismic transient processes due to dilatancy recovery [*Jónsson et al.*, 2003; *Fialko*, 2004], afterslip [*Froment et al.*, 2013], and viscoelastic relaxation all follow similar logarithmic decay patterns. However, it is difficult to unambiguously associate an observed logarithmic velocity recovery with a specific physical mechanism and/or depth [*Obermann et al.*, 2013; *Obermann et al.*, 2016; *Yang et al.*, 2019] since all of the processes that influence the subsurface damage zone and post-seismic transients operate on similar timescales. For example, both the healing of the fault zone [*Y. G. Li et al.*, 1998] and decay time of post-seismic deformation [*Fialko*, 2004] are on the order of several years for the 1992 M_w 7.3 Landers Earthquake.

W. Yu et al. [2013b; a] detected repeating earthquakes (REs) near the Sumatra Subduction Zone and used these repeaters to probe the temporal changes in seismic velocity induced by the 2004 M_w 9.2 Sumatra and 2005 M_w 8.6 Nias earthquakes during 2005–2008. They found that the temporal velocity changes in the high-frequency (HF, 0.5−2.0 Hz) *S*-wave codas (δV_S) and long-period (LP, 0.03−0.1 Hz) Rayleigh waves (δV_{LR}) followed similar logarithmic recovery timescales after the 2004 and 2005 earthquakes that were potentially linked to strong GM-induced surface damage or/and post-seismic afterslip. However, the ability to distinguish the velocity changes induced by deep processes from healing of the subsurface damage zone remains a challenge, as mentioned above.

Cracks produced by a previous earthquake can multiply within the subsurface damage zone as a result of the strong GM induced by subsequent earthquakes [*Rubinstein and Beroza*, 2004a]. If the logarithmic velocity recovery reflects healing of the subsurface damage zone, then the re-damage process from subsequent large earthquakes could result in further reduction of the seismic velocity, reversing the established recovery pattern [*Vidale and Li*, 2003; *Rubinstein and Beroza*, 2004a; *Sawazaki et al.*, 2018]. However, velocity recovery is likely to continue without reversal if it is driven by post-seismic afterslip or other deep processes, even in the event of another earthquake. Therefore, the ability to detect such a bifurcation in the temporal velocity recovery patterns would help discriminate between the healing of surface damage zones and slow deformation in the crust.

The 2004 M_w 9.2 Sumatra Earthquake [*Ammon et al.*, 2005; *Park et al.*, 2005; *Subarya et al.*, 2006; *Chlieh et al.*, 2007] has been followed by a series of large earthquakes that have occurred in the proximity of the 2004 rupture zone and in the Wharton Basin, northeast Indian Ocean (Fig. 1; see Table S1 for the event IDs). Examples of the former include the 2005 M_w 8.6 Nias Earthquake [*Hsu et al.*, 2006; *Ishii et al.*, 2007; *Konca et al.*, 2007], 2007 M_w 8.4 and M_w 7.9 Bengkulu double

earthquakes [*Konca et al.*, 2008; *Tsang et al.*, 2016], 2008 M_w 7.3 Simeulue Earthquake [*Morgan et al.*, 2017], and 2010 M_w 7.8 Banyak Earthquake, and examples of the latter include the 2012 M_w 8.6 and M_w 8.2 double earthquakes [*Yue et al.*, 2012; *Wei et al.*, 2013; *Hill et al.*, 2015]. The strong GM generated by these large earthquakes can repeatedly damage the surface layer and interrupt healing, whereas the large post-seismic afterslip from the 2004 M_w 8.8 Sumatra and 2005 M_w 8.2 Nias events [*Hsu et al.*, 2006; *Chlieh et al.*, 2007; *Hoechner et al.*, 2011; *Feng et al.*, 2015] (Fig. 1), among other slow deformation processes, potentially drives continuous velocity changes. The main goal of this work is to examine how seismic-velocity change measurements from different attributes can help differentiate between these concurrent processes.

We extend our previous work [*W. Yu et al.*, 2013a] by incorporating seven additional years of regional seismic waveform data, which expands our RE dataset to the 2005–2015 time period. We discuss the data processing procedures, and summarize the observed temporal velocity changes in δV_S and δV_{LR} in the following sections, where we highlight a clear bifurcation in the δV_S and δV_{LR} patterns: δV_S follows a monotonic logarithmic recovery, while δV_{LR} deviates from the background recovery rate in late 2007. We then investigate the sensitivity of the seismic velocity model to the first-order pattern of the observed lag-time time series $\tau(t)$ of the HF *S*-coda and LP Rayleigh waves using a series of perturbed velocity models.

2. Seismic data, and $\tau(t)$ and δV measurements

2.1 Repeating earthquakes recorded by seismographic station PSI

The procedural details for the RE detection and relative location assessment within a given earthquake sequence have been discussed in previous studies [*Wen*, 2006; *W. Yu and Wen*, 2012; *W.*

135 *Yu*, 2013; *W. Yu et al.*, 2013b]. Several previously identified RE sequences continued to occur in the
136 afterslip zones of the 2004 and 2005 earthquakes until the end of 2015 (Fig. 1). The high-precision
137 relative hypocenter locations of these REs (relative to the estimated rupture area of the selected RE
138 sequences) are presented in the Supporting Information (Text S1, Fig. S1, and Table S2).
139 Seismographic station PSI, which was installed in Parapat, Sumatra, Indonesia, in 1993, is equipped
140 with a Streckeisen STS-2 broadband sensor. Station PSI detected the REs immediately after the 2004
141 and 2005 mainshocks, and it is in an advantageous position to potentially detect the δV induced by
142 the 2005 event since the seismic waves from the RE sequences associated with the 2005 event
143 propagated through the main slip and surface damage zones of the 2005 event as they traveled to
144 station PSI.

145

146 **2.2 $\tau(t)$ measurements using coda wave interferometry**

147 Coda wave interferometry is used to measure the $\tau(t)$ of the HF *S*-coda and LP Rayleigh waves
148 relative to the direct *P*-wave onset in a given RE sequence [*Poupinet et al.*, 1984; *Snieder et al.*, 2002;
149 *Snieder*, 2006]. The HF waveforms are convolved using a zero-phase two-pole Butterworth bandpass
150 filter with 0.5 and 2.0 Hz corner frequencies, and the LP Rayleigh waves are bandpass filtered
151 between 0.03 and 0.1 Hz. The reference event of a given RE sequence is chosen as the last event
152 before late 2007, when the onset of an additional increase in the Rayleigh-wave lag times (τ_{LR}) is
153 detected (to be discussed in Section 3). We measure the differential time of the first 4-s HF *P*-wave
154 between the target and reference events via the cross correlation (CC) of each RE pair. We adopt 4-
155 and 40-s sliding windows for the HF coda and LP surface waves, respectively, with a 95% overlap
156 between successive time windows for both waves. The $\tau(t)$ for the HF *S*-coda and LP Rayleigh waves
157 are computed as the time differences between either the HF *S*-coda or LP Rayleigh waves, and the
158 HF *P*-wave onset using a sliding-window CC approach. A 50-ms sampling interval of the original
159 time series is interpolated to a 5-ms sampling interval to achieve subsample precision in time. Note

that the subsample precision can also be attained by interpolating the resulting CC time series. We find that the $\tau(t)$ calculated via CC of the interpolated time series is identical to that obtained via interpolation of the resulting CC time series. The $\tau(t)$ for the HF *S*-coda waves (τ_S) can be expressed as follows:

$$t_S = (t^{trg}_{S\text{-}coda} - t^{ref}_{S\text{-}coda}) - (t^{trg}_{HF\,P} - t^{ref}_{HF\,P}), \quad (1)$$

where t refers to the arrival times (or lapse times) of the 4-s HF *P*- (subscripted "HF *P*") and *S*-coda (subscripted "*S*-coda") waves between the target (superscripted "trg") and reference (superscripted "ref") events of a given RE pair. The $\tau(t)$ for the 20-s dominant period (LP) Rayleigh waves (τ_{LR}) can be expressed as follows:

$$t_{LR} = (t^{trg}_{20sLR} - t^{ref}_{20sLR}) - (t^{trg}_{HF\,P} - t^{ref}_{HF\,P}). \quad (2)$$

The $\tau(t)$ measurements can eliminate the uncertainties due to the relative origin time error of the event catalog and Global Positioning System (GPS) clock drift error between the two events in a given RE pair. The earthquake-induced crustal velocity reduction could also influence the arrival time of the direct *P*-wave from the target events and introduce a bias in $\tau(t)$. The direct *P*-wave is insensitive to the medium changes compared with the later part of the coda [*Poupinet et al.*, 1984; *Snieder et al.*, 2002] and Rayleigh waves since it has the shortest propagation path. Figures 2a and 2c display example HF coda and LP Rayleigh waveforms from the N1 RE sequence that were recorded by station PSI, respectively, with the waveforms of the target events aligned via CC of the 4-s HF *P*-wave between the target and reference events. Figures 2b and 2d display the calculated $\tau(t)$ of the HF coda and LP Rayleigh waves from the corresponding waveforms displayed in Figures 2a and 2c, respectively. Signal-to-noise ratios (SNRs) are used to sort the time segments with sufficient signal strength, and are defined as follows: the noise amplitude is measured as the maximum amplitude in the 5–15-s time window before the *P*-wave arrival, and the signal amplitude is measured as the maximum amplitude in a given time window. *W. Yu et al.* [2013a] previously adopted SNR thresholds of 5 for HF *S*-coda waves and 10 for LP Rayleigh waves. However, a minimum threshold of SNR = 10 with this new data set would exclude many τ_{LR} measurements, yielding few temporal

Field Code Changed

samples for the RE sequences. Therefore, we explore suitable SNR thresholds for the LP Rayleigh waves of smaller events. We find that a threshold requiring at least 80% of the 40-s lapse time segments (i.e., 32 s) to satisfy SNR of ≥5, and a CC coefficient of ≥0.9 between each waveform pair yields a reasonable number of τ_{LR} measurements and stable τ_{LR} values. We acquire 471 $\tau(t)$ measurements from the HF *S*-coda and LP Rayleigh waves using the above-mentioned SNR and CC thresholds.

2.3 δV_S and δV_{LR} measurements and uncertainties

The assumption of a spatially homogenous velocity reduction relative to the background velocity allows the δV centered at lapse time t to be estimated as follows [*Snieder et al.*, 2002]:

$$dV = -\frac{t(t)}{t}. \quad (3)$$

The observed $\tau_S(t)$ for the 2005 Nias Earthquake RE sequences is stretched in the later part of the coda waves, similar to previous findings [*Poupinet et al.*, 1984; *Lobkis and Weaver*, 2003]. A fractional seismic-velocity change in the *S*-wave coda (δV_S) of the RE pair can be approximated by a negative $\tau_S(t)$ slope (dashed lines in Fig. 2b). Linear regression is used to estimate the parameters of the slope b ($-\delta V_S$) and intercept a whose τ_S values that meet the SNR and CC coefficient thresholds. The 2σ standard deviations in δV_S are twice the computed root mean square (RMS) of $\tau_{iS} - \widehat{\tau}_{iS}$, where $\widehat{\tau}_{iS} = a + bt_i$, which is the predicted value based on the inferred a and b values. However, τ_{LR} is constant for the entire wave packet (Fig. 2d). The fractional velocity change for the LP Rayleigh wave (δV_{LR}) is computed as follows:

$$dV_{LR} = -\frac{\overline{t_{LR}}}{t_{LR}}, \quad (4)$$

Field Code Changed

Field Code Changed

Field Code Changed

Field Code Changed

where $\overline{t_{LR}}$ is the mean of the τ_{LR} lapse time segments that satisfy the SNR and CC coefficient thresholds, and t_{LR} is the Rayleigh-wave arrival time. The 2σ standard deviations in δV_{LR} are twice the computed RMS of t_{iLR} - $\overline{t_{LR}}$ (Fig. 3 and the following figures).

Field Code Changed

Field Code Changed

We emphasize that δV_S and δV_{LR} are used to highlight the time-dependent discrepancy in late 2007. If the upper crust experiences partial or uniform velocity perturbations induced by earthquake slip, then one would anticipate detectable changes in both the *P*- and *S*-coda waves. We observe that the τ_P values are smaller than the τ_S values and only detectable immediately after the Nias Earthquake (see Section 3). Therefore, we only focus on δV_S and δV_{LR} in our analysis. We consider the effect of fractional changes in both the *P*- and *S*-wave velocities of the crust and how the velocity model perturbations influence the synthetic $\tau(t)$ results (see Section 4).

3. Temporal changes in δV_S and δV_{LR}: observations of bifurcation

We examine the $\tau_S(t)$ from the N1 sequence at station PSI to determine the decade-long temporal evolution of δV_S and δV_{LR} (Figs. 2 and 3). The τ_S values of the first target event (15 April 2005) increase monotonically to τ_S = +0.07 s (light-blue curve in Fig. 2b) relative to the 9 October 2006 reference event, which is equivalent to δV_S = −0.1% (dashed black line in Fig. 2b). The slope of τ_S decreases with time. However, the τ_S values for the 2 July 2008 target event decrease to about −0.02 s (red curve in Fig. 2b), which is equivalent to δV_S = +0.02% (dashed light-red line). δV_S exhibits a continuous recovery between 2005 and 2011 that amounts to ~0.14% (Fig. 3a).

The τ_{LR} value for the first target event (15 April 2005) is about +0.16 s (light-blue curve in Fig. 2d), and then decreases to +0.11 s for the 3 December 2005 event. However, the τ_{LR} values increase to +0.44 s for the subsequent 2 July 2008 and 29 March 2011 target events (red and blue curves in Fig. 2d, respectively). δV_{LR} recovered from −0.13% to −0.09% between 15 April 2005 and 3 December 2005, but then decreased to −0.36% between 9 October 2006 and 2 July 2008, which is almost three times greater than the change in δV_{LR} in the three weeks following the 2005 Nias mainshock. These observations therefore include a clear break from the observed recovery trend after the 2007 Bengkulu and 2008 Simeulue earthquakes (Fig. 3b).

Similar discrepancies between τ_S and τ_{LR} are consistently detected among all of the Sumatra and Nias RE sequences at station PSI after late 2007 (Fig. 4). Note that the $\tau(t)$ values for the S1 and S4 Sumatra RE sequences possess smaller values and fluctuate around zero for the HF coda waves (Fig. 4e and g). The monotonic increase in the HF *P*-wave coda lag times (τ_P) only holds for the target events that occurred within the first week following the 2005 Nias Earthquake, with calculated τ_P values of up to +0.03 s (thick light-blue curves in Figs. 4c and 5b−g). Because the τ_P values are a factor of two smaller than the τ_S values (e.g., Fig. 3a of *W. Yu et al.* [2013a]) to begin with, given the same decay rate, the τ_P values largely decreased to zero after the first week following the 2005 mainshock (Figs. 4a and 5a).

We use a kernel density estimation [*Parzen*, 1962] with adequate bandwidths that are adopted to both assess the overall distribution of the δV_S and δV_{LR} measurements whose time separations are longer than half a year, and establish the consistency and robustness of the observed δV_S and δV_{LR} trends (Fig. 3c and d). The kernel density estimation is a representation of the probability density function and can be formulated as follows:

$$\widehat{f}_h(x) = \frac{1}{n}\sum_{i=1}^{n} K\left(\frac{x - x_i}{h}\right), \quad (5)$$

where x_i is the i-th δV data of the total sample size n, h is the bandwidth value that controls the smoothness of the resulting probability density curve, and $K(x_i, h)$ is the kernel expressed in Gaussian function:

$$K(x_i, h) = \frac{1}{h\sqrt{2\pi}} e^{-\frac{1}{2}\left(\frac{x - x_i}{h}\right)^2}. \quad (6)$$

The peaks correspond to the maximum likelihood values for each set of δV data. Note that the break from the δV_{LR} recovery after late 2007 is likely caused by both the 2007 and 2008 earthquakes (to be discussed in Section 5). We adopt the timing of the 2007 Bengkulu earthquakes to sort the δV values into two groups, before (blue curve, group 1) and across the 2007 earthquakes (red curve, group 2); the 2007 earthquakes were simply chosen for this division since they occurred first. We observe a noticeable contrast between the group 1 and group 2 δV values. The peak δV_S value changes from −0.04% in group 1 to +0.007% in group 2, indicating continuous velocity recovery (Fig. 3c), whereas the peak δV_{LR} value changes from −0.16% in group 1 to −0.25% in group 2, indicating an additional velocity reduction and minimum recovery after 2007 (Fig. 3d). The post-2007 δV_{LR} values (group 2) are typically a factor of two larger than those measured earlier in the time series (group 1). The steady δV_S recovery at station PSI after the 2004/2005 earthquakes is consistent among all of the Sumatra and Nias RE sequences (left panels of Figs. 6 and 7). The δV_{LR} values consistently exhibit substantial offsets of −0.3 to −0.6% for all of the RE sequences across the late 2007 timeframe (right panels of Figs. 6 and 7). We conclude that this is a robust observation of clear bifurcation in the temporal δV_{LR} and δV_S variations.

4. Finite-difference synthetics and $\tau(t)$ examination

The finite-difference (FD) method [*Helmberger and Vidale*, 1988; *Vidale and Helmberger*, 1988] is used to compute the synthetic seismograms. Our goal is to explore the seismic velocity model parameters that are sensitive to the first-order pattern of the observed τ_S and τ_{LR} trends. Our one-dimensional (1D) reference velocity model, termed "mST2", is a combination of the ST2 model (upper 50 km) [*Lange et al.*, 2010] and isotropic Preliminary reference Earth model (PREM; 50–370 km depth) [*Dziewonski and Anderson*, 1981]. The ST2 velocity model is derived from regional *P*- and *S*-wave travel times whose phases sampled the Sumatra Subduction Zone. Here we perturb the *P*-wave velocity (α), *S*-wave velocity (β), and layer thickness of the mST2 model for our sensitivity analysis (Fig. 8a and b). Random media are adopted for all of the models, which are defined by Gaussian correlation functions with RMS perturbations and correlation lengths in the *x*- and *z*-directions (*clx* and *clz*, respectively) [*Frankel and Clayton*, 1986]. A two-dimensional (2D) random-media reference velocity model is formed from the 1D mST2 velocity model using the following parameters: RMS = 10%, *clx* = 0.5 km, and *clz* = 0.5 km (isotropic, with an aspect ratio *clx*/*clz* = 1; see Table 1). We consider two end-member models, "deep layer" (DL) and "surface" (SF). The settings for the DL models include superposed background velocity $d\alpha$ and $d\beta$ perturbations, and variations in the *clx*/*clz* aspect ratio and RMS in the upper 1–16 km of the crust, whereas the settings for the SF models include superposed $d\beta$ perturbations, *clx*/*clz*, and RMS variations that are confined to the uppermost 0.5–1.0 km. The perturbed parameters for each model are presented in Table 1.

We consider the geometry of the N1 sequence recorded at station PSI for most of the computations, with a 22-km focal depth for the N1 RE sequence and 267-km epicentral distance from station PSI. The dimensions of the FD regime are 500 km × 220 km (*x*-direction × *z*-direction), and the length of the time window is 170 s, with a 0.0625-km grid spacing and 3.125-ms time step used during the computation. The source is positioned at x = 100 km and z = 22 km. The random-media regime extends from x = 101.5 km to x = 500 km and from z = 0 km to z = 1 km for SF models, and

299 from z = 1 km to z = 16 km for DL models (Fig. 8c). The FD synthetics are accurate up to 6.0 Hz.
300 We also present two examples where we consider the geometry of the S1 sequence at station PSI,
301 with a 48-km focal depth for the S1 RE sequence and 534-km epicentral distance from station PSI.
302 The dimensions of the FD regime are 900 km × 370 km (x-direction × z-direction) for the S1–PSI
303 geometry, and the length of the time window is 280 s, with a 0.125-km grid spacing and 6.25-ms
304 time step. The source is positioned at x = 100 km and z = 48 km. The precision of the synthetic
305 seismograms for S1 is accurate up to 3.0 Hz. *clz* is fixed at 0.5 km, meaning each scatterer includes
306 four and eight grid cells in the z-direction for the S1–PSI and N1–PSI regimes, respectively. We use
307 a dip-slip focal mechanism and 1-s triangle source time function. The HF synthetic seismograms are
308 bandpass filtered between 0.4 and 1.6 Hz. The synthetic $\tau(t)$ values that are computed from the
309 synthetic seismograms are based on the perturbed models relative to the reference model using a
310 sliding-window CC approach, which is identical to the approach used to obtain the observed $\tau(t)$
311 values.

312

313 The heterogeneous regions that can produce the observed time-dependent time delay include a
314 localized velocity reduction near either the source or station, and a velocity reduction in the bulk of
315 the upper crust. We first examine the effect of a localized velocity reduction near either the source
316 or station. The N1 DL-LSRC1 model produces τ_P values of up to +0.05 s and null τ_S values for a
317 localized velocity reduction near the source (orange curve in Fig. 9a), whereas the N1 SF-LSRC1
318 model produces null τ_P and τ_S values (light-blue curve in Fig. 9a). The N1 SF-LSTN1 model produces
319 null τ_P and τ_S values for a localized velocity reduction near the station (thick green curve in Fig. 9a),
320 and the S1 SF-LSTN1 model produces oscillating τ_P and τ_S values between −0.05 s and +0.05 s for
321 the S1–PSI path (thick green curve in Fig. 10a). Amplifying the localized S-wave velocity reduction
322 near the station from $d\beta$ = –4% to −16% produces a linear increase in $\tau_S(t)$ values, with increases of
323 +0.075 s (N1 SF-LSTN2; thick yellow curve in Fig. 9a) and +0.15 s (S1 SF-LSTN2; thick yellow

curve in Fig. 10a), respectively, for the N1 and S1 sequences recorded by station PSI. Two lines of argument suggest that the observed $\tau(t)$ values of the HF *S*-coda waves are not caused by a localized near-surface velocity reduction at station PSI. (1) The perturbed models with localized velocity perturbations near the station produce a linear increase in τ_S values, even at different distance ranges, whereas the observed τ_S values for the S1 sequence at station PSI does not exhibit an increase in $\tau_S(t)$ (light-blue curve in Fig. 4e). (2) A monotonic increase in τ_P values is detectable for the target events that occurred within the first week following the Nias mainshock (Figs. 4b and 5b−g), but the smaller τ_P values largely diminished to zero after the first week following the Nias Earthquake. The observed τ_P and τ_S values suggest that the velocity reduction occurs in the bulk part of the upper crust. Moreover, the localized velocity reduction near either the source or station produces null τ_{LR} values (Figs. 9c and 10c).

Here we discuss how the velocity reduction parameters, RMS perturbations, and *clx*/*clz* aspect ratio for the SF and DL models influence the synthetic $\tau(t)$ values for the HF *S*-coda and Rayleigh waves. The following FD synthetics computations employ the N1–PSI source–receiver geometry. Figure 11 displays the synthetic test results where an individual parameter is moderately perturbed, such that the sensitivity of each perturbed parameter can be assessed. Models SF1, SF2, and SF3 have a 3% RMS amplification, increase in the *clx*/*clz* ratio from one to ten, and additional $d\beta = -4\%$ perturbation relative to the reference model, respectively. The synthetic $\tau(t)$ values for the HF *S*-coda waves that propagated through these models all exhibit subtle fluctuations around zero, with episodic oscillations at 10, 20–30, and 47–52 s (Fig. 11a). Models DL1, DL2, and DL3 have a 3% RMS amplification, increase in the *clx*/*clz* aspect ratio from one to ten, and additional $d\alpha = -0.06\%$ and $d\beta = -0.12\%$ perturbations relative to the reference model, respectively. The 3% RMS amplification also produces subtle fluctuations in the τ_P and τ_S values (DL1, light-blue curve in Fig. 11c). However, increasing the *clx*/*clz* aspect ratio from one to ten produces a negative τ_S value of −0.07 s at ~50 s

(DL2, orange curve in Fig. 11c), and the $d\alpha = -0.06\%$ and $d\beta = -0.12\%$ perturbations produce an increase in the τ_S value of up to +0.13 s (DL3, pink curve in Fig. 11c). Model DL4, which includes all of the perturbations in models DL1, DL2, and DL3, produces a monotonic increase in τ_P, as well as smaller τ_S values at ~50 s (green curve in Fig. 11c). The smaller τ_S values mimic the negative τ_S values in the DL2 model at 47–52 s due to the increase in the *clx*/*clz* aspect ratio.

We now consider the effects of RMS amplification and perturbing several parameters within a given velocity model. A monotonic increase in both $\tau_P(t)$ and $\tau_S(t)$ is still better approximated by the DL models for the HF *P*- and *S*-wave codas (DL5 and DL6 in Fig. 12c). The SF models with a strong *S*-wave velocity reduction ($d\beta = -16\%$) produce oscillating $\tau_P(t)$ and $\tau_S(t)$ values with peaks at 10, 20−30, and 47−52 s (SF5 and SF6 in Fig. 12a). The DL models with RMS = 25%, $d\alpha = -0.06\%$, $d\beta = -0.12\%$ perturbations, and *clx*/*clz* = 1 produces linear increases of up to +0.072 and +0.147 s in τ_P and τ_S, respectively (DL5, light-blue curve in Fig. 12c; the 2D $d\beta$ profile is displayed in Fig. 8d). The τ_P values increase by a factor of 1.5 when the *clx*/*clz* aspect ratio is increased to ten, with a value of up to 0.11 s; the τ_S values are larger up to +0.138 s over the 40−45-s window, but then decrease over the 47−52-s window (DL6, orange curve in Fig. 12c; the 2D $d\beta$ profile is displayed in Fig. 8e). This τ_S pattern of an increase followed by a drop over the 47−52-s window is similar to that observed for models DL3 and DL4 (Fig. 11c). The heterogeneous region in model DL7 only spans 50% of that in model DL5; its predicted τ_P values exhibit an increase over the 10−20-s window to +0.025 s, followed by a drop over the 20−30-s window to −0.03 s, whereas the τ_S values exhibit a monotonic increase up to +0.1 s (DL7, pink curve in Fig. 12c). The combined perturbations of the SF and DL models produce τ_P and τ_S values that are similar to those based calculated from the DL models, with larger τ_P and smaller τ_S values often obtained (Fig. 12e; the 2D $d\beta$ profile of model SF4+DL7 is displayed in Fig. 8f).

373

374 LP Rayleigh waves are sensitive to $d\beta$ reductions and RMS amplification in the bulk crust, with
375 models SF3, SF4, DL3, and DL4 producing τ_{LR} values of +0.087, +0.087, +0.038, and +0.05 s,
376 respectively (Figs. 11e, f, and 12g). Models SF5 and SF6 produce τ_{LR} values in the +0.244 to +0.431
377 s range (Fig. 12g). Models DL5–DL7 have fixed RMS = 25%, $d\alpha = -0.06\%$, and $d\beta = -0.12\%$
378 perturbation; an increase in the *clx*/*clz* aspect ratio from one to ten produces an increase in τ_{LR} from
379 +0.125 s (DL5) to +0.150 s (DL6), whereas a reduction in the heterogeneous region in model DL7
380 produces a maximum τ_{LR} value of only +0.056 s (Fig. 12h). Combinations of the SF4 model and
381 various DL models have also been used to produce synthetic τ_{LR} values, with τ_{LR} values of +0.219,
382 +0.250, and +0.156 s obtained for models SF4+DL5, SF4+DL6, and SF4+DL7, respectively (Fig.
383 12i).

384

385 Our modeling results indicate that a strong *S*-wave velocity reduction in the near-surface
386 substantially contributes to the large τ_{LR} values, but has a minimal effect on the observed τ_P and τ_S
387 pattern. A subtle *S*-wave velocity reduction in the upper crust is necessary to account for the observed
388 τ_P and τ_S patterns, and can also partially contribute to the τ_{LR} pattern. Our preferred explanation is as
389 follows. The observed τ_S and τ_{LR} patterns after the 2004/2005 earthquakes may reflect the
390 combination of a strong *S*-wave velocity reduction in the near-surface and a subtle *S*-wave velocity
391 reduction in the upper crust. However, the τ_{LR} amplification after late 2007 predominantly reflects
392 another substantial *S*-wave velocity reduction in the near-surface, given the null τ_S constraint (red
393 curves in Fig. 4). The medium changing from isotropic (*clx*/*clz* = 1) to vertically transverse isotropic
394 (*clx*/*clz* = 10) and amplifying the RMS can influence *S*-coda and Rayleigh-wave propagation, thereby
395 altering the τ_S and τ_{LR} values. We discuss the likely scenarios that can potentially explain these
396 observations and modeling results in the following section.

5. Discussion and Conclusions

5.1 δV_S recovery after the 2004 and 2005 earthquakes

Obermann et al. [2013] positioned the source and receiver at the surface in their coda wave computations, and suggested that the later part of the coda waves were predominantly sensitive to the bulk velocity heterogeneities of the media, with the sensitivity of these waves to the source depth being approximately bounded by the length scale of the mean free path. Here we position the source and receiver at 22 km depth and the surface, respectively, in our FD simulations. Our FD synthetic tests reveal that the DL models with subtle *S*-wave velocity perturbations that are confined to the upper 1–16 km produce characteristics that are consistent with a monotonic increase in τ_S (Fig. 12c), whereas the SF models with near-surface velocity perturbations (confined to the uppermost 0.5−1.0 km) cannot reproduce this key feature (Fig. 12a). Although the source–receiver geometries of the two modeling approaches are different, our inferences on the sensitivity of the later part of the coda waves to the bulk heterogeneities of the media are consistent with those in *Obermann et al*. [2013].

The δV_S observations show continuous recovery from 2005 to 2015. It is unlikely that the δV_S induced by co-seismic slip would be sustained for several years, even though the deformation induced by large earthquake co-seismic slip can produce structural changes in the bulk crust and time-varying δV_S behavior. Additional independent arguments suggest that the continuous δV_S recovery from 2005 to 2015 was predominantly controlled by deep post-seismic afterslip or/and viscoelastic relaxation processes. The REs associated with the 2004 and 2005 earthquakes are located close to the afterslip zones, at depths of about 50 and 25 km, respectively (Fig. 1 and Table S2). The post-seismic displacement time series recorded by GPS stations UMLH and LEWK, and the GPS normalized displacement time series relative to the concurrent δV_S values are provided in Figures S2 and S3,

421 respectively, for comparison. Note that the details of the GPS data processing can be found in *Feng*
422 *et al.* [2015]. The logarithmic recovery of δV_S corresponds to the post-seismic deformation time
423 series reasonably well. *Feng et al.* [2015] suggested that viscoelastic relaxation was essential for
424 explaining the long-term geodetic measurements. *Qiu et al.* [2018] recently estimated a background
425 upper mantle viscosity of 10^{17}–10^{19} Pa-s beneath the Sumatra region, which would indicate relaxation
426 timescales (days to years) that are similar to our observed timescales of δV_S recovery.

427

428 **5.2 Multiple δV_{LR} reductions induced by the 2004, 2005, 2007, and 2008 earthquakes**

429 The observed δV_{LR} values at station PSI from late 2007 to early 2008 exhibit a remarkable
430 reduction of at least −0.3%, which is a factor of two larger than the reductions caused by the 2004
431 and 2005 earthquakes (Figs. 3, 6, and 7). These new data reveal that the δV_{LR} reduction after the 2004,
432 2005, 2007, and 2008 earthquakes progressively increases, i.e., $\delta V_{LR}^{2007/2008} > \delta V_{LR}^{2005} > \delta V_{LR}^{2004}$.
433 Note that substantial δV_{LR} reductions are likely caused by the 2007 M_w 8.4 and M_w 7.9, and 2008
434 earthquakes. It is difficult to assess the temporal resolution of δV_{LR} using the RE sequences due to
435 the undersampling during the five-month period when the 2007 and 2008 earthquakes occurred.
436 Previous studies have suggested that earthquake-induced velocity reduction is often associated with
437 high PGV [*Rubinstein and Beroza*, 2004b; *Hobiger et al.*, 2016]. We examine the PGV of the large
438 earthquakes recorded by station PSI in the 0.5–2.0 Hz frequency band (Table S3). The PGV
439 amplitude of the 2005 M_w 8.6 earthquake is larger than that of the 2004 M_w 9.2 event, and the PGV
440 amplitudes of the 2007 M_w 8.4 and M_w 7.9, and 2008 M_w 7.3 earthquakes are smaller than those of
441 the 2005 M_w 8.6 event, even though a stronger δV_{LR} reduction that is associated with the 2007 and
442 2008 earthquakes is detected. We speculate that the strong GM induced by the 2004 and 2005 events
443 made the subsurface cracks and fractures more susceptible to the GM induced by the 2007 and 2008
444 earthquakes, resulting in another substantial velocity reduction.

445

446 **5.3 Temporal changes in δV during 2005−2015**

447 REs discretely sample δV with a limited temporal resolution. However, concurrent δV_S and
448 δV_{LR} observations, and the differences in their temporal patterns offer new insights into the diverse
449 processes that modulate media properties. Figure 13 summarizes the decadal δV_S and δV_{LR}
450 observations, and illustrates our inferences on the evolution of the crustal seismic-velocity structure
451 along the Banda Aceh−Nias−Simeulue segment of the Sumatra Subduction Zone. A subtle −0.1%
452 δV_S reduction due to the 2004 and/or 2005 earthquakes is followed by steady recovery, with no
453 noticeable disruption from 2005 to 2015 (δV_S in Fig. 13). However, a −0.1% δV_{LR} reduction is
454 induced by the 2004 earthquake, and a slightly larger −0.1 to −0.3% reduction is induced by the 2005
455 event. We find that δV_{LR} experiences recovery until late 2007, with the GM from the 2007 and 2008
456 earthquakes then inducing a substantial δV_{LR} reduction (−0.3 to −0.6%) that possibly occurred in
457 multiple steps. We speculate that any δV_{LR} caused by the 2010 Banyak Earthquake may have gone
458 undetected due to the limited temporal resolution of the data, resulting in the observed gentle velocity
459 recovery trend.

460

461 In summary, the differences in the temporal δV_S and δV_{LR} behaviors that are inferred from
462 REs are a powerful tool for discriminating between the mechanisms that drive seismic-velocity
463 changes after great earthquakes. Steady δV_S recovery is consistent with the logarithmic time
464 dependence inferred from post-seismic GPS data (Figs. S2 and S3), which predominantly reflects
465 afterslip that occurred in the updip and downdip sections of the rupture area [*Feng et al.*, 2015] (Fig.
466 1) and/or viscoelastic relaxation after the 2004 and 2005 earthquakes. Furthermore, FD synthetics
467 computations demonstrate that the monotonic increase in the observed τ_S values can be explained by
468 a subtle velocity reduction of $d\beta = -0.12\%$ at 1−16 km depth (DL5 in Fig. 12c). However, δV_{LR}

displays additional drops after the large earthquakes during the 2007−2008 time period, breaking the pattern of monotonic recovery. The model with a subtle *S*-wave velocity reduction at 1−16 km depth can partly account for the observed τ_{LR} pattern after the 2004/2005 events, but it is insufficient in producing values that are comparable to the observed τ_{LR} pattern after late 2007. Strong *S*-wave velocity reductions of $d\beta = -4$ and −16% that are confined to the uppermost 0.5−1.0 km can account for the observed τ_{LR} values after 2005 and late 2007, respectively (Fig. 12g). These sudden changes are primarily associated with a cycle of damage, healing, and re-damage in the subsurface layer [*Vidale and Li*, 2003; *Sawazaki et al.*, 2018].

Acknowledgments

The seismic data analyzed in this paper were assembled from the PS network, which were downloaded from the JAMSTEC data center, Japan (http://p21.jamstec.go.jp/top/; last accessed on 23 August 2019). W.Y. wishes to thank Lujia Feng of the Earth Observatory of Singapore (EOS), Nanyang Technological University (NTU), for providing the processed GPS displacement time series presented in the study, and Louisa L. H. Tsang of EOS, NTU, for providing the slip model for the 2007 Bengkulu Earthquake. We thank Kathryn Materna and an anonymous reviewer for constructive reviews. W.Y. also wishes to thank Haekal A. Haridhi, Chi-Hsien Tang, and Bor-Shouh Huang of Academia Sinica, Chun-Hsiang Kuo of the National Center for Research on Earthquake Engineering, and Shengji Wei of EOS, NTU, for insightful discussions. This study was supported by the Institute of Earth Sciences, Academia Sinica, and grants MOST-104-2116-M-001-010-, MOST-106-2116-M-001-009-, and MOST-107-2116-M-001-014- from the Ministry of Science and Technology, Taiwan, Republic of China. T.R.A.S. acknowledges support from the Natural Environment Research Council (NE/P001378/1), United Kingdom.

492 **References**
493

494 Ammon, C. J., C. Ji, H. K. Thio, D. Robinson, S. D. Ni, V. Hjorleifsdottir *et al.* (2005), Rupture
495 process of the 2004 Sumatra–Andaman earthquake. *Science*, *308* (5725), 1133–1139.
496 doi:10.1126/science.1112260.
497 Barbot, S., and Y. Fialko (2010), A unified continuum representation of post-seismic relaxation
498 mechanisms: semi-analytic models of afterslip, poroelastic rebound and viscoelastic flow.
499 *Geophys. J. Int.*, *182* (3), 1124–1140. doi:10.1111/j.1365-246X.2010.04678.x.
500 Bird, P. (2003), An updated digital model of plate boundaries. *Geochem. Geophys. Geosys.*, *4* (3),
501 doi:10.1029/2001GC000252.
502 Brenguier, F., M. Campillo, C. Hadziioannou, N. M. Shapiro, R. M. Nadeau, and E. Larose (2008),
503 Postseismic relaxation along the San Andreas fault at Parkfield from continuous
504 seismological observations. *Science*, *321* (5895), 1478–1481. doi:10.1126/science.1160943.
505 Chlieh, M., J. P. Avouac, V. Hjorleifsdottir, T. R. A. Song, C. Ji, K. Sieh *et al.* (2007), Coseismic
506 slip and afterslip of the great Mw 9.15 Sumatra–Andaman earthquake of 2004. *Bull. Seismol.*
507 *Soc. Am.*, *97* (1A), S152–S173. doi:10.1785/0120050631.
508 Dziewonski, A. M., and D. L. Anderson (1981), Preliminary Reference Earth Model. *Phys. Earth*
509 *Planet. Inter.*, *25* (4), 297−356.
510 Feng, L. J., E. M. Hill, P. Banerjee, I. Hermawan, L. L. H. Tsang, D. H. Natawidjaja *et al.* (2015), A
511 unified GPS-based earthquake catalog for the Sumatran plate boundary between 2002 and
512 2013. *J. Geophys. Res. Solid Earth*, *120* (5), 3566−3598. doi:10.1002/2014JB011661.
513 Fialko, Y. (2004), Evidence of fluid-filled upper crust from observations of postseismic deformation
514 due to the 1992 Mw7.3 Landers earthquake. *J. Geophys. Res.*, *109* (B8),
515 doi:10.1029/2004JB002985.
516 Fielding, E. J., P. R. Lundgren, R. Bürgmann, and G. J. Funning (2009), Shallow fault-zone dilatancy
517 recovery after the 2003 Bam earthquake in Iran. *Nature*, *458*, 64–68.
518 doi:10.1038/nature07817.
519 Frankel, A., and R. W. Clayton (1986), Finite-difference simulations of seismic scattering:
520 Implications for the propagation of short-period seismic waves in the crust and models of
521 crustal heterogeneity. *J. Geophys. Res.*, *91* (B6), 6465–6489.
522 Froment, B., M. Campillo, J. H. Chen, and Q. Y. Liu (2013), Deformation at depth associated with
523 the 12 May 2008 MW 7.9 Wenchuan earthquake from seismic ambient noise monitoring.
524 *Geophys. Res. Lett.*, *40* (1), 78–82. doi:10.1029/2012GL053995.
525 Gudmundsson, Ó., and M. Sambridge (1998), A regionalized upper mantle (RUM) seismic model.
526 *J. Geophys. Res.*, *103* (B4), 7121–7136. doi:10.1029/97JB02488.

527 Helmberger, D. V., and J. E. Vidale (1988), Modeling strong motions produced by earthquakes with
528 two-dimensional numerical codes. *Bull. Seismol. Soc. Am.*, *78* (1), 109–121.
529 Hill, E. M., H. Yue, S. Barbot, T. Lay, P. Tapponnier, I. Hermawan *et al.* (2015), The 2012 Mw 8.6
530 Wharton Basin sequence: A cascade of great earthquakes generated by near-orthogonal,
531 young, oceanic mantle faults. *J. Geophys. Res. Solid Earth*, *120* (5), 3723–3747.
532 doi:10.1002/2014JB011703.
533 Hobiger, M., U. Wegler, K. Shiomi, and H. Nakahara (2016), Coseismic and post-seismic velocity
534 changes detected by Passive Image Interferometry: comparison of one great and five strong
535 earthquakes in Japan. *Geophys. J. Int.*, *205* (2), 1053–1073. doi:10.1093/gji/ggw066.
536 Hoechner, A., S. V. Sobolev, I. Einarsson, and R. J. Wang (2011), Investigation on afterslip and
537 steady state and transient rheology based on postseismic deformation and geoid change
538 caused by the Sumatra 2004 earthquake. *Geochem. Geophys. Geosys.*, *12* (Q07010),
539 doi:10.1029/2010GC003450.
540 Hsu, Y. J., M. Simons, J. P. Avouac, J. Galetzka, K. Sieh, M. Chlieh *et al.* (2006), Frictional afterslip
541 following the 2005 Nias–Simeulue earthquake, Sumatra. *Science*, *312* (5782), 1921–1926.
542 doi:10.1126/science.1126960.
543 Ishii, M., P. M. Shearer, H. Houston, and J. E. Vidale (2007), Teleseismic P wave imaging of the 26
544 December 2004 Sumatra-Andaman and 28 March 2005 Sumatra earthquake ruptures using
545 the Hi-net array. *J. Geophys. Res.*, *112* (B11307), doi:10.1029/2006JB004700.
546 Jónsson, S., P. Segall, R. Pedersen, and G. Björnsson (2003), Post-earthquake ground movements
547 correlated to pore-pressure transients. *Nature*, *424*, 179–183. doi:10.1038/nature01776.
548 Konca, A. O., V. Hjorleifsdottir, T. R. A. Song, J. P. Avouac, D. V. Helmberger, C. Ji *et al.* (2007),
549 Rupture kinematics of the 2005 Mw 8.6 Nias–Simeulue earthquake from the joint inversion
550 of seismic and geodetic data. *Bull. Seismol. Soc. Am.*, *97* (1A), S307–S322.
551 doi:10.1785/0120050632.
552 Konca, A. O., J. P. Avouac, A. Sladen, A. J. Meltzner, K. Sieh, P. Fang *et al.* (2008), Partial rupture
553 of a locked patch of the Sumatra megathrust during the 2007 earthquake sequence. *Nature*,
554 *456*, 631–635. doi:10.1038/nature07572.
555 Lange, D., F. Tilmann, A. Rietbrock, R. Collings, D. H. Natawidjaja, B. W. Suwargadi *et al.* (2010),
556 The fine structure of the subducted Investigator Fracture Zone in Western Sumatra as seen
557 by local seismicity. *Earth Planet. Sci. Lett.*, *298* (1−2), 47−56.
558 doi:10.1016/j.epsl.2010.07.020.
559 Li, L., F. L. Niu, Q. F. Chen, J. R. Su, and J. B. He (2017), Post-seismic velocity changes along the
560 2008 M7.9 Wenchuan earthquake rupture zone revealed by S coda of repeating events.
561 *Geophys. J. Int.*, *208* (2), 1237–1249. doi:10.1093/gji/ggw454.

562 Li, Y. G., J. E. Vidale, K. Aki, F. Xu, and T. Burdette (1998), Evidence of shallow fault zone
563 strengthening after the 1992 M7.5 Landers, California, earthquake. *Science*, *279* (5348), 217–
564 219.
565 Li, Y. G., P. Chen, E. S. Cochran, J. E. Vidale, and T. Burdette (2006), Seismic evidence for rock
566 damage and healing on the San Andreas fault associated with the 2004 M 6.0 Parkfield
567 earthquake. *Bull. Seismol. Soc. Am.*, *96* (4B), S349–S363. doi:10.1785/0120050803.
568 Lobkis, O. I., and R. L. Weaver (2003), Coda-wave interferometry in finite solids: Recovery of P-to-
569 S conversion rates in an elastodynamic billiard. *Phys. Rev. Lett.*, *90* (25),
570 doi:10.1103/PhysRevLett.90.254302.
571 Morgan, P. M., L. J. Feng, A. J. Meltzner, E. O. Lindsey, L. L. H. Tsang, and E. M. Hill (2017),
572 Sibling earthquakes generated within a persistent rupture barrier on the Sunda megathrust
573 under Simeulue Island. *Geophys. Res. Lett.*, *44* (5), 2159–2166. doi:10.1002/2016GL071901.
574 Obermann, A., T. Planès, E. Larose, C. Sens-Schönfelder, and M. Campillo (2013), Depth sensitivity
575 of seismic coda waves to velocity perturbations in an elastic heterogeneous medium. *Geophys.*
576 *J. Int.*, *194* (1), 372–382. doi:10.1093/gji/ggt043.
577 Obermann, A., T. Planès, C. Hadziioannou, and M. Campillo (2016), Lapse-time-dependent coda-
578 wave depth sensitivity to local velocity perturbations in 3-D heterogeneous elastic media.
579 *Geophys. J. Int.*, *207* (1), 59–66. doi:10.1093/gji/ggw264.
580 Park, J., T. R. A. Song, J. Tromp, E. Okal, S. Stein, G. Roult *et al.* (2005), Earth's free oscillations
581 excited by the 26 December 2004 Sumatra–Andaman earthquake. *Science*, *308* (5725), 1139–
582 1144. doi:10.1126/science.1112305.
583 Parzen, E. (1962), On estimation of a probability density function and mode. *Annals of Mathematical*
584 *Statistics*, *33* (3), 1065−1076.
585 Peltzer, G., P. Rosen, F. Rogez, and K. Hudnut (1996), Postseismic rebound in fault step-overs
586 caused by pore fluid flow. *Science*, *273* (5279), 1202–1204.
587 Peng, Z. G., and Y. Ben-Zion (2006), Temporal changes of shallow seismic velocity around the
588 Karadere-Düzce branch of the North Anatolian fault and strong ground motion. *Pure Appl.*
589 *Geophys.*, *163*, 567–600. doi:10.1007/s00024-005-0034-6.
590 Poupinet, G., W. L. Ellsworth, and J. Frechet (1984), Monitoring velocity variations in the crust using
591 earthquake doublets : An application to the Calaveras Fault, California. *J. Geophys. Res.*, *89*
592 (B7), 5719–5731.
593 Qiu, Q., J. D. P. Moore, S. Barbot, L. J. Feng, and E. M. Hill (2018), Transient rheology of the
594 Sumatran mantle wedge revealed by a decade of great earthquakes. *Nat. Commun.*, *9*.
595 doi:10.1038/s41467-018-03298-6.

596 Rivet, D., M. Campillo, N. M. Shapiro, V. Cruz-Atienza, M. Radiguet, N. Cotte *et al.* (2011), Seismic
597 evidence of nonlinear crustal deformation during a large slow slip event in Mexico. *Geophys.*
598 *Res. Lett.*, *38* (L08308), doi:10.1029/2011GL047151.
599 Rubinstein, J. L., and G. C. Beroza (2004a), Nonlinear strong ground motion in the ML 5.4
600 Chittenden earthquake: Evidence that preexisting damage increases susceptibility to further
601 damage. *Geophys. Res. Lett.*, *31* (L23614), doi:10.1029/2004GL021357.
602 Rubinstein, J. L., and G. C. Beroza (2004b), Evidence for widespread nonlinear strong ground motion
603 in the Mw 6.9 Loma Prieta Earthquake. *Bull. Seismol. Soc. Am.*, *94* (5), 1595–1608.
604 doi:10.1785/012004009.
605 Rubinstein, J. L., N. Uchida, and G. C. Beroza (2007), Seismic velocity reductions caused by the
606 2003 Tokachi-Oki earthquake. *J. Geophys. Res.*, *112* (B05315), doi:10.1029/2006JB004440.
607 Sawazaki, K., H. Kimura, K. Shiomi, N. Uchida, R. Takagi, and R. Snieder (2015), Depth-
608 dependence of seismic velocity change associated with the 2011 Tohoku earthquake, Japan,
609 revealed from repeating earthquake analysis and finite-difference wave propagation
610 simulation. *Geophys. J. Int.*, *201* (2), 741–763. doi:10.1093/gji/ggv014.
611 Sawazaki, K., T. Saito, and K. Shiomi (2018), Shallow temporal changes in *S* wave velocity and
612 polarization anisotropy associated with the 2016 Kumamoto earthquake sequence, Japan. *J.*
613 *Geophys. Res. Solid Earth*, *123* (11), 9899−9913. doi:10.1029/2018JB016261.
614 Schaff, D. P., and G. C. Beroza (2004), Coseismic and postseismic velocity changes measured by
615 repeating earthquakes. *J. Geophys. Res.*, *109* (B10302), doi:10.1029/2004JB003011.
616 Snieder, R., A. Grêt, H. Douma, and J. Scales (2002), Coda wave interferometry for estimating
617 nonlinear behavior in seismic velocity. *Science*, *295* (5563), 2253–2255.
618 doi:10.1126/science.1070015.
619 Snieder, R. (2006), The theory of coda wave interferometry. *Pure Appl. Geophys.*, *163*, 455–473.
620 doi:10.1007/s00024-005-0026-6.
621 Snieder, R., C. Sens-Schönfelder, and R. J. Wu (2017), The time dependence of rock healing as a
622 universal relaxation process, a tutorial. *Geophys. J. Int.*, *208* (1), 1−9. doi:10.1093/gji/ggw377.
623 Subarya, C., M. Chlieh, L. Prawirodirdjo, J. P. Avouac, Y. Bock, K. Sieh *et al.* (2006), Plate-
624 boundary deformation associated with the great Sumatra–Andaman earthquake. *Nature*, *440*,
625 46–51. doi:10.1038/nature04522.
626 Takagi, R., T. Okada, H. Nakahara, N. Umino, and A. Hasegawa (2012), Coseismic velocity change
627 in and around the focal region of the 2008 Iwate-Miyagi Nairiku earthquake. *J. Geophys. Res.*,
628 *117* (B6), doi:10.1029/2012JB009252.

Tang, C. H., Y. J. Hsu, S. Barbot, J. D. P. Moore, and W. L. Chang (2019), Lower-crustal rheology and thermal gradient in the Taiwan orogenic belt illuminated by the 1999 Chi-Chi earthquake. *Sci. Adv.*, *5* (2), doi:10.1126/sciadv.aav3287.

TenCate, J. A., E. Smith, and R. A. Guyer (2000), Universal slow dynamics in granular solids. *Phys. Rev. Lett.*, *85* (5), 1020−1023.

Tsang, L. L. H., E. M. Hill, S. Barbot, Q. Qiu, L. J. Feng, I. Hermawan *et al.* (2016), Afterslip following the 2007 Mw 8.4 Bengkulu earthquake in Sumatra loaded the 2010 Mw 7.8 Mentawai tsunami earthquake rupture zone. *J. Geophys. Res. Solid Earth*, *121* (12), 9034–9049. doi:10.1002/2016JB013432.

Vidale, J. E., and D. V. Helmberger (1988), Elastic finite-difference modeling of the 1971 San Fernando, California earthquake. *Bull. Seismol. Soc. Am.*, *78* (1), 122–141.

Vidale, J. E., and Y. G. Li (2003), Damage to the shallow Landers fault from the nearby Hector Mine earthquake. *Nature*, *421*, 524–526. doi:10.1038/nature01354.

Wegler, U., H. Nakahara, C. Sens-Schöenfelder, M. Korn, and K. Shiomi (2009), Sudden drop of seismic velocity after the 2004 Mw 6.6 mid-Niigata earthquake, Japan, observed with Passive Image Interferometry. *J. Geophys. Res.*, *114* (B06305), doi:10.1029/2008JB005869.

Wei, S. J., D. Helmberger, and J. P. Avouac (2013), Modeling the 2012 Wharton basin earthquakes off-Sumatra: Complete lithospheric failure. *J. Geophys. Res. Solid Earth*, *118* (7), 3592–3609. doi:10.1002/jgrb.50267.

Wen, L. (2006), Localized temporal change of the Earth's inner core boundary. *Science*, *314* (5801), 967–970. doi:10.1126/science.1131692.

Wu, C. Q., Z. G. Peng, and Y. Ben-Zion (2009), Non-linearity and temporal changes of fault zone site response associated with strong ground motion. *Geophys. J. Int.*, *176* (1), 265–278. doi:10.1111/j.1365-246X.2008.04005.x.

Yang, C., G. Li, F. Niu, and Y. Ben-Zion (2019), Significant effects of shallow seismic and stress properties on phase velocities of Rayleigh waves up to 20 s. *Pure Appl. Geophys.*, *176*, 1255–1267. doi:10.1007/s00024-018-2075-7.

Yu, T., and S. H. Hung (2012), Temporal changes of seismic velocity associated with the 2006 Mw 6.1 Taitung earthquake in an arc-continent collision suture zone. *Geophys. Res. Lett.*, *39* (L12307), doi:10.1029/2012GL051970.

Yu, W., and L. Wen (2012), Deep-focus repeating earthquakes in the Tonga–Fiji subduction zone. *Bull. Seismol. Soc. Am.*, *102* (4), 1829–1849. doi:10.1785/0120110272.

Yu, W. (2013), Shallow-focus repeating earthquakes in the Tonga–Kermadec–Vanuatu subduction zones. *Bull. Seismol. Soc. Am.*, *103* (1), 463–486. doi:10.1785/0120120123.

Yu, W., T. R. A. Song, and P. G. Silver (2013a), Temporal velocity changes in the crust associated with the great Sumatra earthquakes. *Bull. Seismol. Soc. Am.*, *103* (5), 2797–2809. doi:10.1785/0120120354.

Yu, W., T. R. A. Song, and P. G. Silver (2013b), Repeating aftershocks of the great 2004 Sumatra and 2005 Nias earthquakes. *J. Asian Earth Sci.*, *67–68*, 153–170. doi:10.1016/j.jseaes.2013.02.018.

Yue, H., T. Lay, and K. D. Koper (2012), En échelon and orthogonal fault ruptures of the 11 April 2012 great intraplate earthquakes. *Nature*, *490*, 245–249. doi:10.1038/nature11492.

Zhao, P., and Z. G. Peng (2009), Depth extent of damage zones around the central Calaveras fault from waveform analysis of repeating earthquakes. *Geophys. J. Int.*, *179* (3), 1817–1830. doi:10.1111/j.1365-246X.2009.04385.x.

676 **List of Figure Captions**

677

678 **Figure 1.** Regional seismicity map of the Sumatra Subduction Zone. The epicenters of several major
679 earthquakes ($M_w \geq 7.3$) are shown as either large open white or black stars that are labeled with their
680 respective event ID or M_w values, respectively (Table S1). The repeating earthquake (RE) sequences
681 are represented by small stars, and the background seismicity is represented by the gray dots, all of
682 which is superimposed on the modeled co-seismic slip (contours) and post-seismic afterslip (colored
683 area) of the 2004 Sumatra [*Chlieh et al.*, 2007] and 2005 Nias [*Hsu et al.*, 2006] earthquakes. Note
684 that color scales for the afterslip values of the 2004 and 2005 events are different. The double arrows
685 show the rupture extents of the 2004 and 2005 events on the map. The REs that were selected for the
686 relative locations and temporal velocity change analyses (Table S2) are indicated by small yellow
687 stars, whereas the REs with high cross-correlation (CC) coefficients and no further relocation
688 analysis are indicated by small white stars; the source parameters of the latter are not provided. The
689 REs are located near the afterslip zones of the 2004 and 2005 events [*Chlieh et al.*, 2007]. The solid
690 and dotted black lines indicate the trench [*Bird*, 2003] and slab depths at 50-km intervals
691 [*Gudmundsson and Sambridge*, 1998], respectively. The seismic and GPS stations used in this
692 analysis are indicated by the open triangle and open squares, respectively. An enlarged map near the
693 Nias, Banyak, and Simeulue Islands is provided to better present the 2005 Nias Earthquake RE
694 locations, with the dotted gray box indicating the location of the displayed region in the main figure.

695

696

Figure 2. (a, c) Waveforms and (b, d) lag-time time series $\tau(t)$ for the N1 RE sequence recorded at station PSI. The vertical-component data are shown for the (a, b) high-frequency (HF) coda waves, bandpass filtered between 0.5 and 2.0 Hz, and (c, d) long-period (LP; 0.03–0.1 Hz) Rayleigh waves. The $\tau(t)$ values for the target event are computed relative to the reference event (black trace, 9 October 2006) and labeled "target event ID–ref". The amplitudes of the filtered waveforms in each selected time window are normalized to the maximum amplitude in that window. The shaded regions correspond to the waveform segments with signal-to-noise ratios (SNR) of ≥5 and cross-correlation (CC) coefficients of ≥0.9, which are used to compute δV. The unstable and oscillatory $\tau(t)$ values at the beginning of each lower plot are due to low SNR values. The dashed black and light-red lines in (b) correspond to the $-\delta V_S$ values that are estimated from the observed $\tau_S(t)$ of the target events: 15 April 2005 (light-blue line) and 2 July 2008 (red line), respectively. The arrival times of the *P*-, *S*-, and LP Rayleigh waves are labeled "P", "S", and "LR", respectively.

Figure 3. Temporal velocity changes in (a) δV_S and (b) δV_{LR}, and their respective standard deviations (error bars) for the N1 RE sequence recorded at station PSI during the 2005−2011 time period, beginning after the 2005 event. The reference event is indicated by the open black triangle and placed on the zero line (baseline). The 2σ standard deviations in δV_S and δV_{LR} are discussed in the text. The vertical dotted lines correspond to the major earthquakes near the Sumatra Subduction Zone, including the 2004, 2005, 2007, 2008, 2010 Banyak, 2010 Mentawai, and 2012 earthquakes (earthquake details listed in Table S1). The (c) δV_S and (d) δV_{LR} distributions, measured from the REs that have been relocated (Table S2) and possess high CC coefficients, and determined using Eqs. (5) and (6). The contrast in δV before and across the 2007 Bengkulu earthquakes, which is inferred from the probability density function for all of the data, resembles the δV distributions constructed from the individual RE sequences.

Figure 4. Observed $\tau(t)$ for the selected target events from four RE sequences, recorded at station PSI: (a, b) N1, (c, d) N11, (e, f) S1, and (g, h) S4. The HF τ_P and τ_S, and LP τ_{LR} are displayed in the left and right panels, respectively. The epicentral distance between each RE sequence and station PSI (in km) is displayed in the titles. The light-blue and green curves are the measured $\tau(t)$ for the target events that occurred after the 2004 and 2005 earthquakes, respectively, whereas the red curve is the measured $\tau(t)$ for the target events that occurred after the 2007 and 2008 earthquakes. The measured $\tau(t)$ for the 3 April 2005 target event of the N11 sequence in (c) indicates detectable τ_P values that are highlighted by the thick light-blue curve. This figure is similar to Figure 2b and d.

Figure 5. Observed $\tau(t)$ of the HF coda waves for the selected target events from seven Nias RE sequences recorded at station PSI: (a) N4, (b) N15, (c) N16, (d) N2, (e) N3, (f) N9, and (g) N10. The thick light-blue curves indicate detectable τ_P values, which are mostly detectable for the target events that occurred within the first week following the 2005 Nias Earthquake. This figure is similar to the left panels of Figure 4.

Figure 6. Temporal δV_S (gray circles) and δV_{LR} (red circles), and their respective standard deviations (black error bars) for six Nias RE sequences recorded at station PSI: (a, b) N4, (c, d) N11, (e, f) N13, (g, h) N15, (i, j) N16, and (k, l) N17, displayed over the 2005–2015 time period to highlight the consistency in both the δV_S recovery and temporal break in δV_{LR} recovery after late 2007. The vertical dotted lines indicate the origin times of the 2004, 2005, 2007, 2008, and 2010 Banyak, 2010 Mentawai, and 2012 earthquakes (Table S1), and the open triangles indicate the reference event for each RE sequence, which are placed at zero (baseline). The 2σ standard deviations in δV_S and δV_{LR} are discussed in the text.

745 **Figure 7.** Computed δV_S and δV_{LR} for the Sumatra RE sequences recorded at station PSI: (a, b) S1,
746 (c, d) S3, and (e, f) S4 over the 2005–2015 time period. The figure symbols are same as in Figure 6.

747

748 **Figure 8.** One-dimensional (a) *P*-wave velocity (α) and (b) *S*-wave velocity (β) structures of the
749 mST2 reference velocity model (gray line), which is modified from the ST2 (dotted black line)
750 [*Lange et al.*, 2010] and PREM [*Dziewonski and Anderson*, 1981] models; the upper 100 km of the
751 velocity model is displayed here. (c–f) Lateral $d\beta$ perturbations of several two-dimensional random-
752 media models: (c) reference model, (d) DL5, (e) DL6, and (f) SF4+DL7. The presented models are
753 adopted for simulating wave propagation from the N1 RE sequence to station PSI. The source (star)
754 and receiver (triangle) in (c) are positioned at (100, 22) and (367, 0), respectively, and the FD regime
755 is displayed from x = 98 to 373 km and z = 0 to 25 km. The FD regime in (d–f) is displayed from x
756 = 100 to 240 km and z = 0 to 18 km. Note that color scales for $d\beta$ perturbations of (e) the DL6 model
757 are different from those of (c, d, f) other models. The perturbed parameters of each presented model
758 are listed in Table 1.

759

760

761 **Figure 9.** (a) Synthetic $\tau(t)$ that were calculated from (b) the HF (0.4–1.6 Hz) FD synthetic
762 seismograms of the N1 sequence recorded at station PSI using models with localized velocity
763 perturbations near either the source or station PSI. The computed synthetic seismograms that are
764 based on the reference model are indicated by the black traces, whereas the computed synthetic
765 seismograms that are based on the perturbed models are indicated by the colored traces and
766 superimposed on the reference synthetic seismograms. The *P*- and *S*-coda time windows are plotted
767 separately to highlight the *P*-codas due to their relatively low amplitudes. The amplitude scales for
768 both the *P*- and *S*-waves are displayed. (c) LP (0.03–0.1 Hz) synthetic τ_{LR} based on the same
769 perturbed models, with the synthetic seismograms based on the reference model (black) and model
770 N1 SF-LSTN2 (yellow) displayed in the inset. The perturbed parameters of each presented model
771 are listed in Table 1.

772

773 **Figure 10.** FD synthetic seismograms and corresponding $\tau(t)$ of the S1 sequence at station PSI based
774 on two models with a localized velocity perturbation near station PSI. The perturbed parameters of
775 each presented model are listed in Table 1. This figure is similar to Figure 9.

776

777 **Figure 11.** HF FD synthetic seismograms and corresponding $\tau(t)$ using several velocity models: (a,
778 b) "surface" (uppermost 1.0 km, denoted as "SF") and (c, d) "deep layer" (1–16 km depth, denoted
779 as "DL") with various RMS, correlation length, $d\alpha$, and $d\beta$ perturbations in the random media.
780 Synthetic LP τ_{LR} based on various (e) SF and (f) DL model perturbations. The LP synthetics in (f)
781 that are computed based on the reference model and model DL4 are indicated by black and green
782 traces, respectively. The perturbed parameters of each presented model are listed in Table 1. This
783 figure is similar to Figure 9.

784

Figure 12. FD synthetic seismograms and corresponding $\tau(t)$ for additional (a, b, g) SF, (c, d, h) DL, and (e, f, i) SF4+DL models. The perturbed parameters of each presented model are listed in Table 1. This figure is similar to Figure 11.

Figure 13. Interpretation of the observed temporal changes in δV_{LR} and δV_S induced by the 2004, 2005, 2007, 2008, 2010, and 2012 earthquakes along the Banda Aceh−Nias−Simeulue segment of the Sumatra Subduction Zone. δV_{LR} recovery occurs until it is interrupted by the 2007 and 2008 events. A question mark is placed next to the drop associated with the 2010 Banyak Earthquake to reflect undersampling. The observations indicate an apparent static offset in δV_{LR} without recovery after the 2007 and 2008 events (dashed dark-gray lines). δV_S is reduced by the 2005 event, and undergoes steady recovery during the 2005−2015 time period, in contrast to the complex time-varying δV_{LR} behavior.

797 **Table 1.** List of models used for the finite-difference synthetics computations, and the associated

798 parameters that were modified to perturb the mST2 reference velocity model.

Model ID	Parameters that were modified to perturb the mST2 reference velocity model
Reference random-media model	RMS = 10%, *clx* = 0.5 km, and *clz* = 0.5 km over the 0−1 and 1−16 km depth ranges for the surface (SF) and deep layer (DL) models, respectively
N1 SF-LSRC1 (Surface)	$d\beta$ = −4%, RMS = 25%, *clx* = 0.5 km, and *clz* = 0.5 km over the 0–1 km depth range, localized to within 25 km of the source
N1 DL-LSRC1 (Deep Layer)	$d\alpha$ = −0.06%, $d\beta$ = −0.12%, RMS = 25%, *clx* = 0.5 km, and *clz* = 0.5 km over the 1−16 km depth range, localized to within 25 km of the source
N1 SF-LSTN1 (Surface)	$d\beta$ = −4%, RMS = 25%, *clx* = 0.5 km, and *clz* = 0.5 km over the 0–1 km depth range, localized to within 10 km of the station
N1 SF-LSTN2 (Surface)	$d\beta$ = −16%, RMS = 25%, *clx* = 0.5 km, and *clz* = 0.5 km over the 0–1 km depth range, localized to within 10 km of the station
S1 SF-LSTN1	Similar to N1 SF-LSTN1, but with a 48-km focal depth and 534-km epicentral distance
S1 SF-LSTN2	Similar to N1 SF-LSTN2, but with a 48-km focal depth and 534-km epicentral distance
SF1 (Surface)	RMS = 13%, *clx* = 0.5 km, and *clz* = 0.5 km over the 0–1 km depth range; i.e., a 3% increase in the RMS perturbation relative to the reference random-media model
SF2 (Surface)	RMS = 10%, *clx* = 5 km, and *clz* = 0.5 km over the 0–1 km depth range; i.e., a ten-fold increase in the *clx*/*clz* aspect ratio relative to the reference random-media model
SF3 (Surface)	$d\beta$ = −4%, RMS = 10%, *clx* = 0.5 km, and *clz* = 0.5 km over the 0–1 km depth range; i.e., an additional $d\beta$ perturbation relative to the reference model
SF4 (Surface)	$d\beta$ = −4%, RMS = 25%, *clx* = 0.5 km, and *clz* = 0.5 km over the 0–1 km depth range
SF5 (Surface)	$d\beta$ = −16%, RMS = 10%, *clx* = 0.5 km, and *clz* = 0.5 km over the 0–0.5 km depth range
SF6 (Surface)	$d\beta$ = −16%, RMS = 10%, *clx* = 0.5 km, and *clz* = 0.5 km over the 0–1 km depth range
DL1 (Deep Layer)	RMS = 13%, *clx* = 0.5 km, and *clz* = 0.5 km over the 1−16 km depth range; i.e., a 3% increase in the RMS perturbation relative to the reference random-media model
DL2 (Deep Layer)	RMS = 10%, *clx* = 5 km, and *clz* = 0.5 km over the 1−16 km depth range; i.e., a ten-fold increase in the *clx*/*clz* aspect ratio relative to the reference random-media model
DL3 (Deep Layer)	$d\alpha$ = −0.06%, $d\beta$ = −0.12%, RMS = 10%, *clx* = 0.5 km, and *clz* = 0.5 km over the 1−16 km depth range; i.e., additional $d\alpha$ and $d\beta$ perturbations relative to the reference random-media model
DL4 (Deep Layer)	Combination of the DL1, DL2, and DL3 models
DL5 (Deep Layer)	$d\alpha$ = −0.06%, $d\beta$ = −0.12%, RMS = 25%, *clx* = 0.5 km, and *clz* = 0.5 km over the 1−16 km depth range
DL6 (Deep Layer)	$d\alpha$ = −0.06%, $d\beta$ = −0.12%, RMS = 25%, *clx* = 5 km, and *clz* = 0.5 km over the 1−16 km depth range
DL7 (Deep Layer)	$d\alpha$ = −0.06%, $d\beta$ = −0.12%, RMS = 25%, *clx* = 0.5 km, and *clz* = 0.5 km over the 1–16 km depth range that is within 130 km of the source

SF4+DL5	Combination of the SF4 and DL5 models
SF4+DL6	Combination of the SF4 and DL6 models
SF4+DL7	Combination of the SF4 and DL7 models

Figure 1.

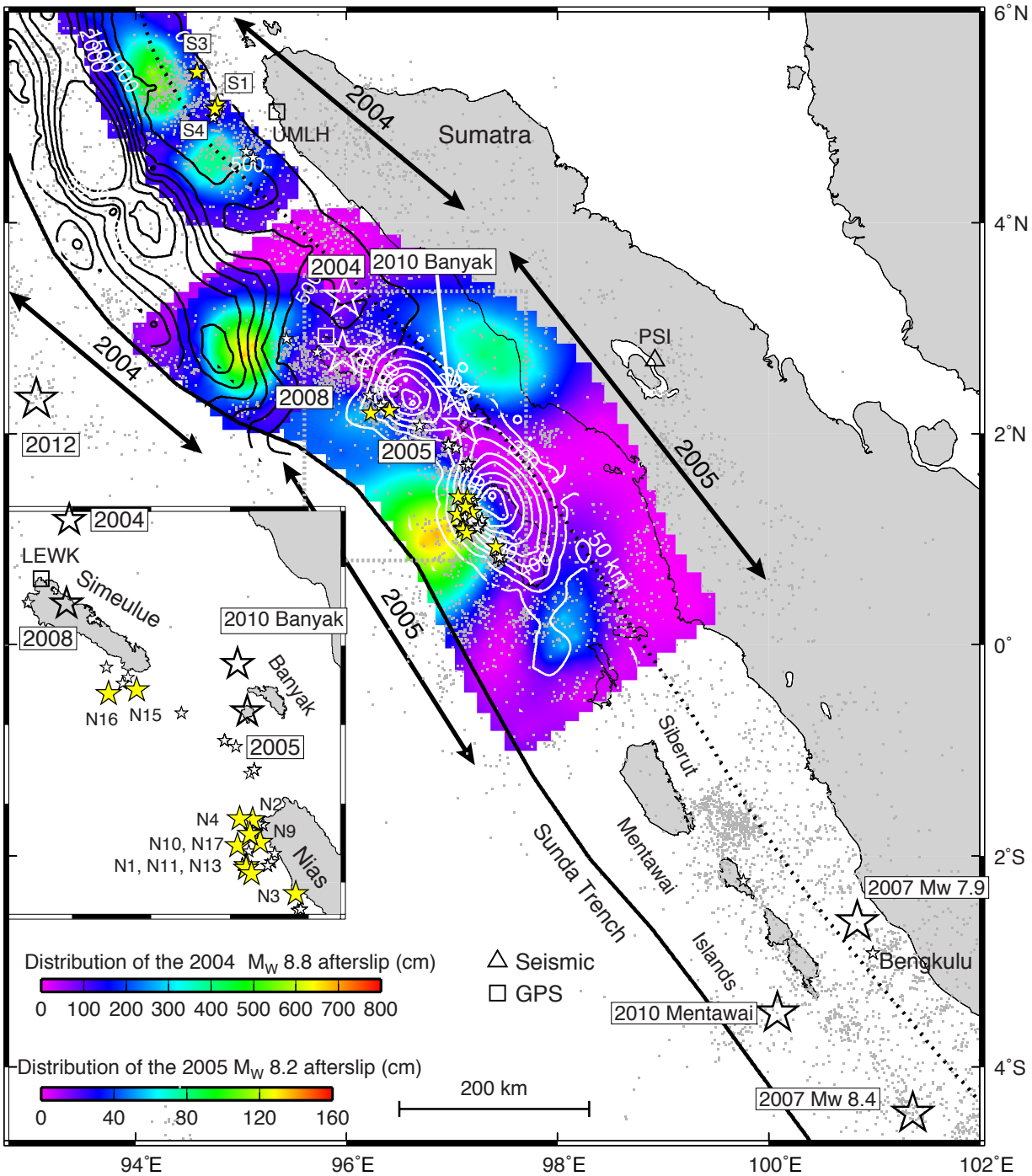
6˚N
4˚N
2˚N
0˚
2˚S
4˚S
94˚E
96˚E
98˚E
100˚E
102˚E
Sumatra
S3
S1
S4
UMLH
2004
2004
2010 Banyak
2004
2012
2008
2005
2005
2005
PSI
50 km
Sunda Trench
Siberut
Mentawai
Islands
2007 Mw 7.9
Bengkulu
2010 Mentawai
2007 Mw 8.4
LEWK
Simeulue
2008
2010 Banyak
Banyak
2005
N16
N15
N2
N4
N9
N10, N17
N1, N11, N13
N3
Nias
Distribution of the 2004 M_W 8.8 afterslip (cm)
0 100 200 300 400 500 600 700 800
Distribution of the 2005 M_W 8.2 afterslip (cm)
0 40 80 120 160
Seismic
GPS
200 km

Figure 2.

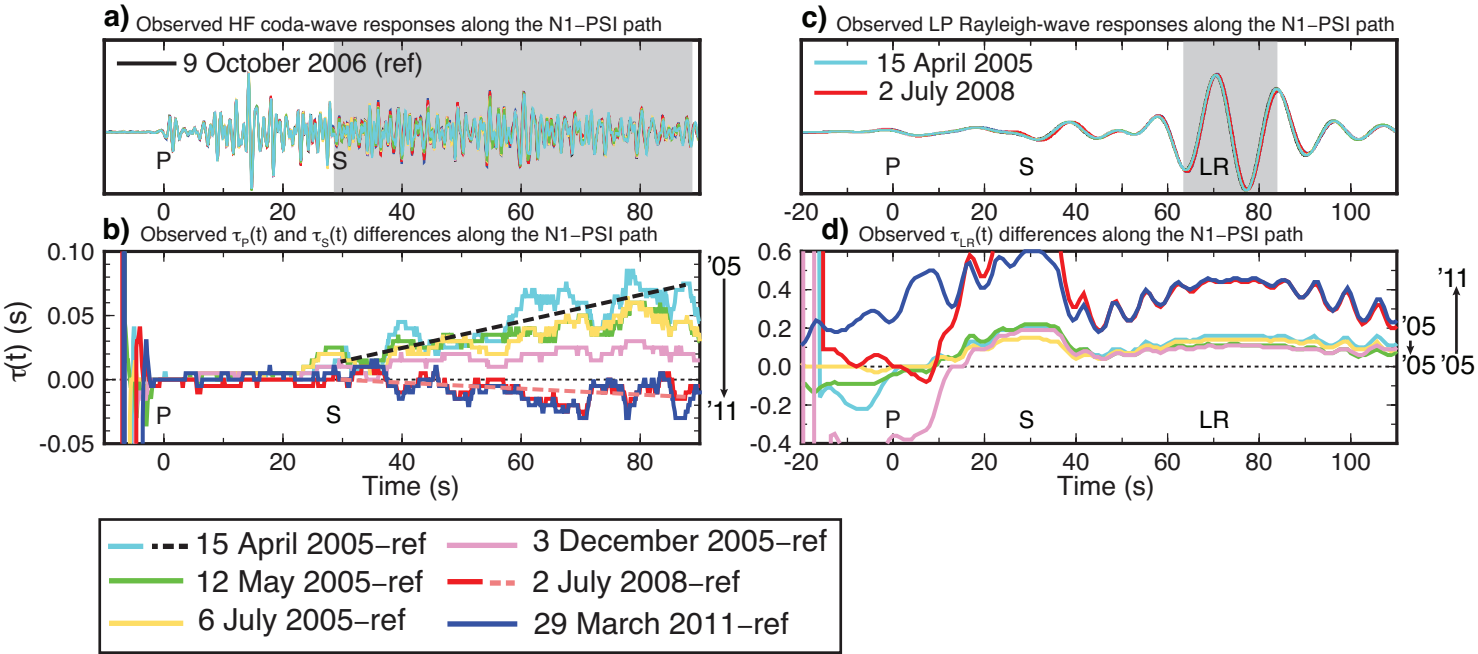
a) Observed HF coda-wave responses along the N1–PSI path
9 October 2006 (ref)
P
S
0
20
40
60
80
b) Observed τP(t) and τS(t) differences along the N1–PSI path
τ(t) (s)
0.10
0.05
0.00
-0.05
P
S
'05
'11
Time (s)
c) Observed LP Rayleigh-wave responses along the N1–PSI path
15 April 2005
2 July 2008
P
S
LR
-20
0
20
40
60
80
100
d) Observed τLR(t) differences along the N1–PSI path
0.6
0.4
0.2
0.0
-0.2
-0.4
'11
'05
'05
'05
P
S
LR
Time (s)
15 April 2005–ref
12 May 2005–ref
6 July 2005–ref
3 December 2005–ref
2 July 2008–ref
29 March 2011–ref

Figure 3.

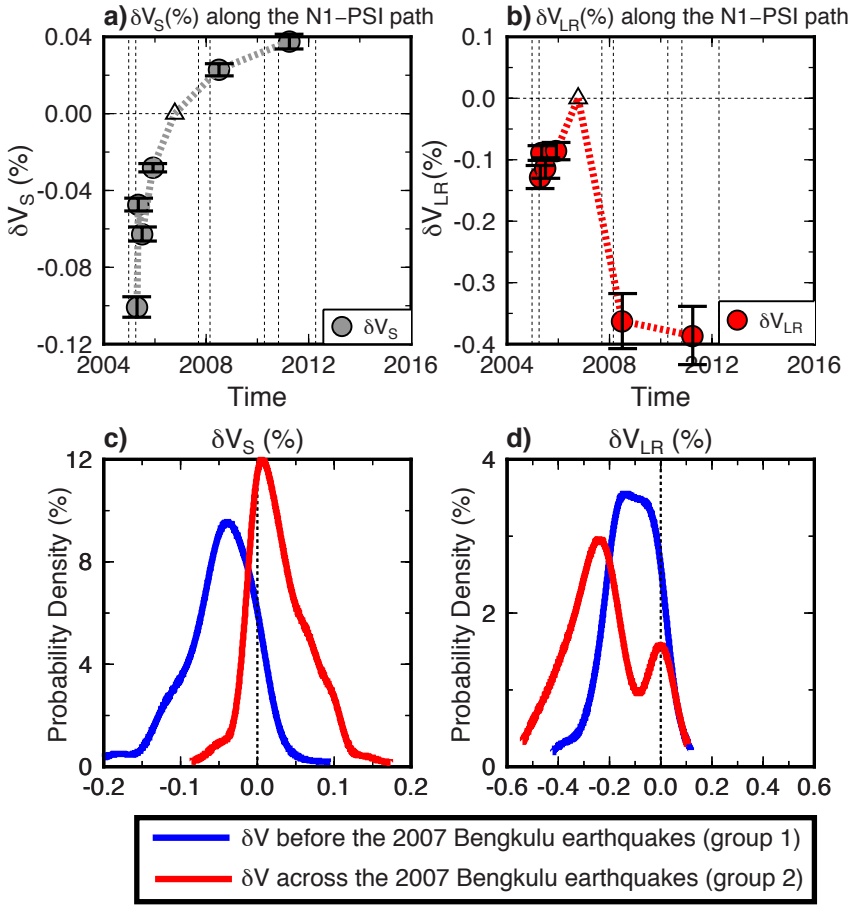
a) δVS(%) along the N1−PSI path
δVS (%)
0.04
0.00
-0.04
-0.08
-0.12
2004
2008
2012
2016
Time
δVS
b) δVLR(%) along the N1−PSI path
δVLR(%)
0.1
0.0
-0.1
-0.2
-0.3
-0.4
2004
2008
2012
2016
Time
δVLR
c)
δVS (%)
Probability Density (%)
12
8
4
0
-0.2
-0.1
0.0
0.1
0.2
d)
δVLR (%)
Probability Density (%)
4
2
0
-0.6
-0.4
-0.2
0.0
0.2
0.4
0.6
δV before the 2007 Bengkulu earthquakes (group 1)
δV across the 2007 Bengkulu earthquakes (group 2)

Figure 4.

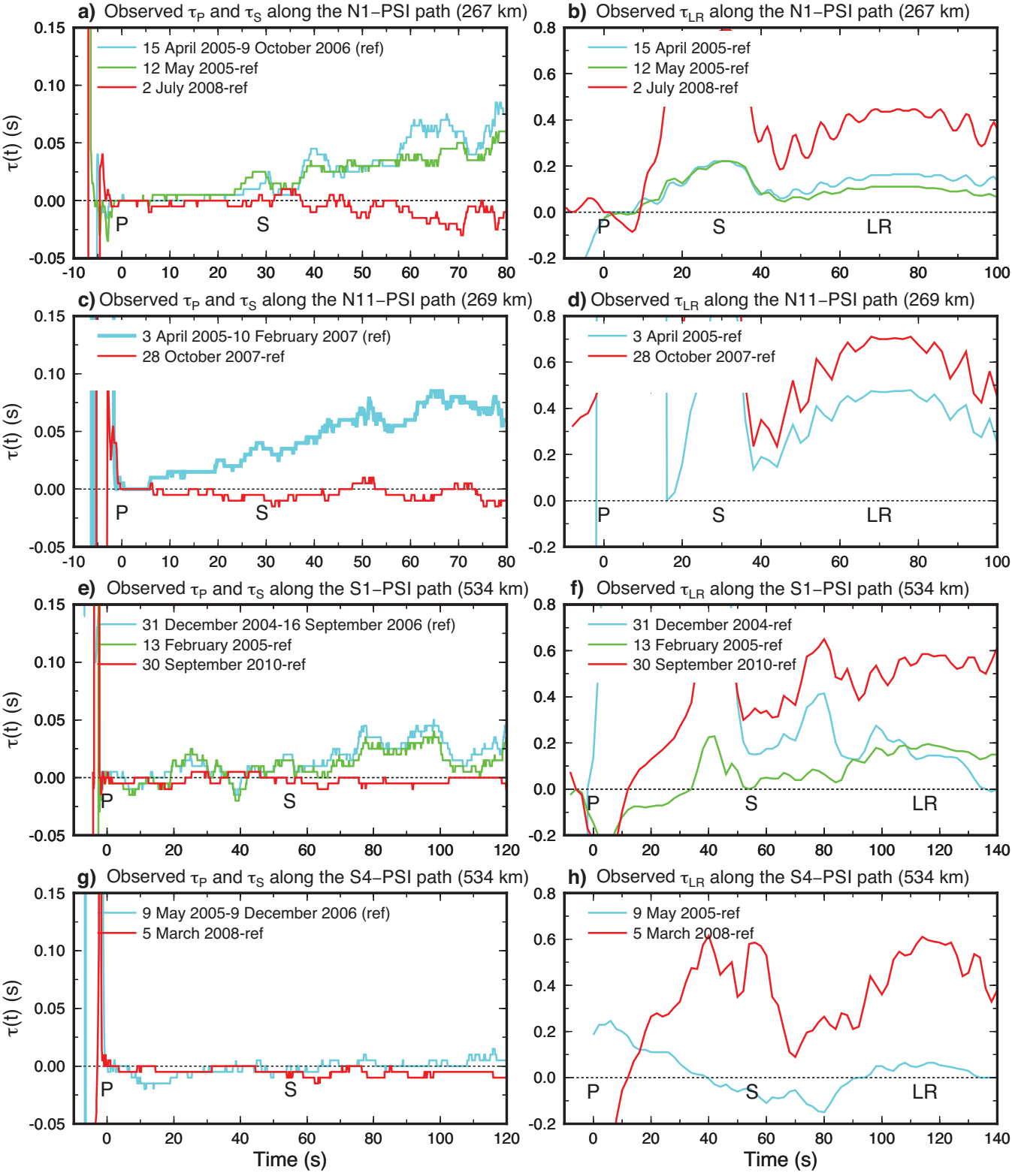
a) Observed τP and τS along the N1–PSI path (267 km)
15 April 2005-9 October 2006 (ref)
12 May 2005-ref
2 July 2008-ref
P
S
b) Observed τLR along the N1–PSI path (267 km)
15 April 2005-ref
12 May 2005-ref
2 July 2008-ref
P
S
LR
c) Observed τP and τS along the N11–PSI path (269 km)
3 April 2005-10 February 2007 (ref)
28 October 2007-ref
P
S
d) Observed τLR along the N11–PSI path (269 km)
3 April 2005-ref
28 October 2007-ref
P
S
LR
e) Observed τP and τS along the S1–PSI path (534 km)
31 December 2004-16 September 2006 (ref)
13 February 2005-ref
30 September 2010-ref
P
S
f) Observed τLR along the S1–PSI path (534 km)
31 December 2004-ref
13 February 2005-ref
30 September 2010-ref
P
S
LR
g) Observed τP and τS along the S4–PSI path (534 km)
9 May 2005-9 December 2006 (ref)
5 March 2008-ref
P
S
h) Observed τLR along the S4–PSI path (534 km)
9 May 2005-ref
5 March 2008-ref
P
S
LR
τ(t) (s)
Time (s)

Figure 5.

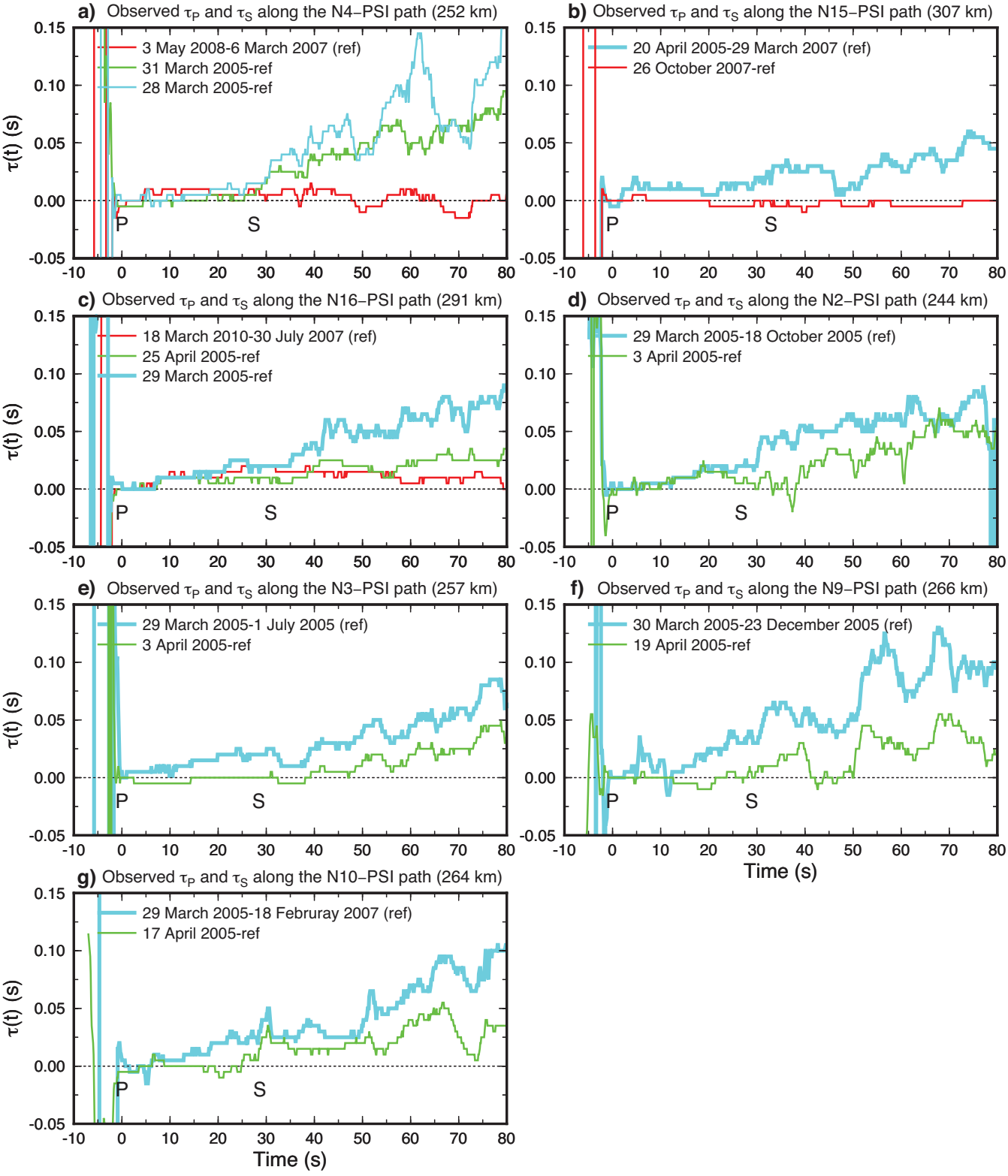
a) Observed τP and τS along the N4–PSI path (252 km)
3 May 2008-6 March 2007 (ref)
31 March 2005-ref
28 March 2005-ref
b) Observed τP and τS along the N15–PSI path (307 km)
20 April 2005-29 March 2007 (ref)
26 October 2007-ref
c) Observed τP and τS along the N16–PSI path (291 km)
18 March 2010-30 July 2007 (ref)
25 April 2005-ref
29 March 2005-ref
d) Observed τP and τS along the N2–PSI path (244 km)
29 March 2005-18 October 2005 (ref)
3 April 2005-ref
e) Observed τP and τS along the N3–PSI path (257 km)
29 March 2005-1 July 2005 (ref)
3 April 2005-ref
f) Observed τP and τS along the N9–PSI path (266 km)
30 March 2005-23 December 2005 (ref)
19 April 2005-ref
g) Observed τP and τS along the N10–PSI path (264 km)
29 March 2005-18 Februray 2007 (ref)
17 April 2005-ref
τ(t) (s)
P
S
Time (s)

Figure 6.

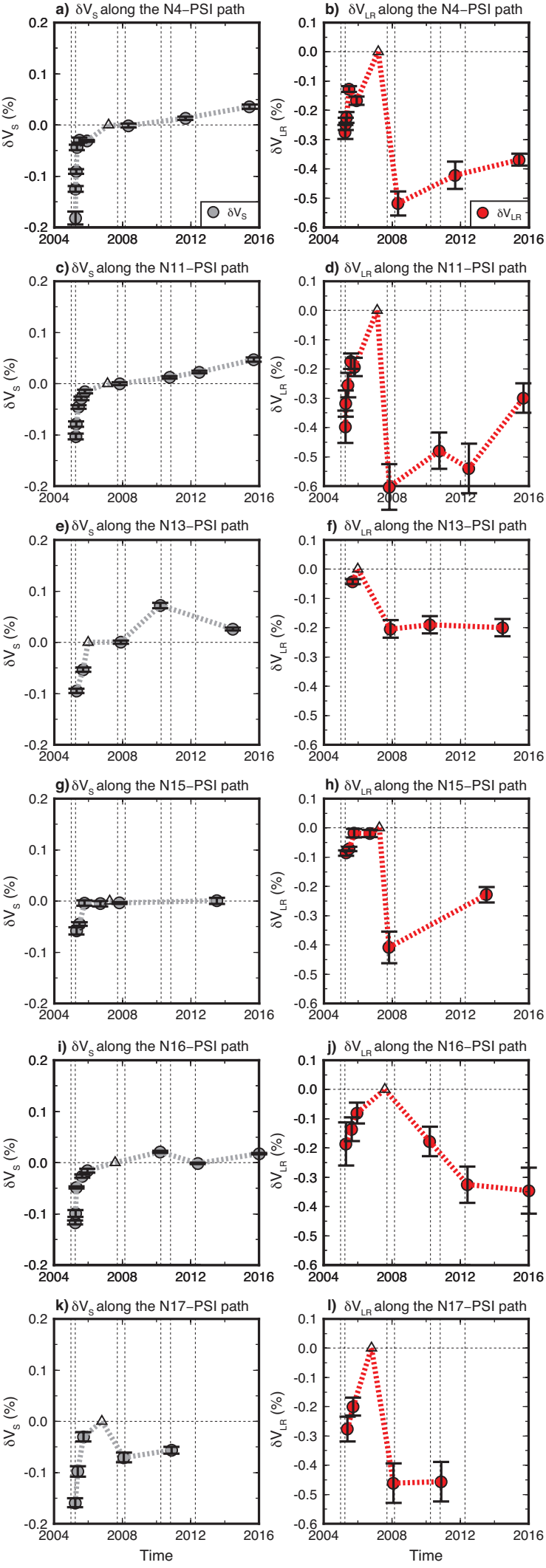
a) δV_S along the N4–PSI path
b) δV_LR along the N4–PSI path
c) δV_S along the N11–PSI path
d) δV_LR along the N11–PSI path
e) δV_S along the N13–PSI path
f) δV_LR along the N13–PSI path
g) δV_S along the N15–PSI path
h) δV_LR along the N15–PSI path
i) δV_S along the N16–PSI path
j) δV_LR along the N16–PSI path
k) δV_S along the N17–PSI path
l) δV_LR along the N17–PSI path
δV_S (%)
δV_LR (%)
δV_S
δV_LR
2004
2008
2012
2016
Time

Figure 7.

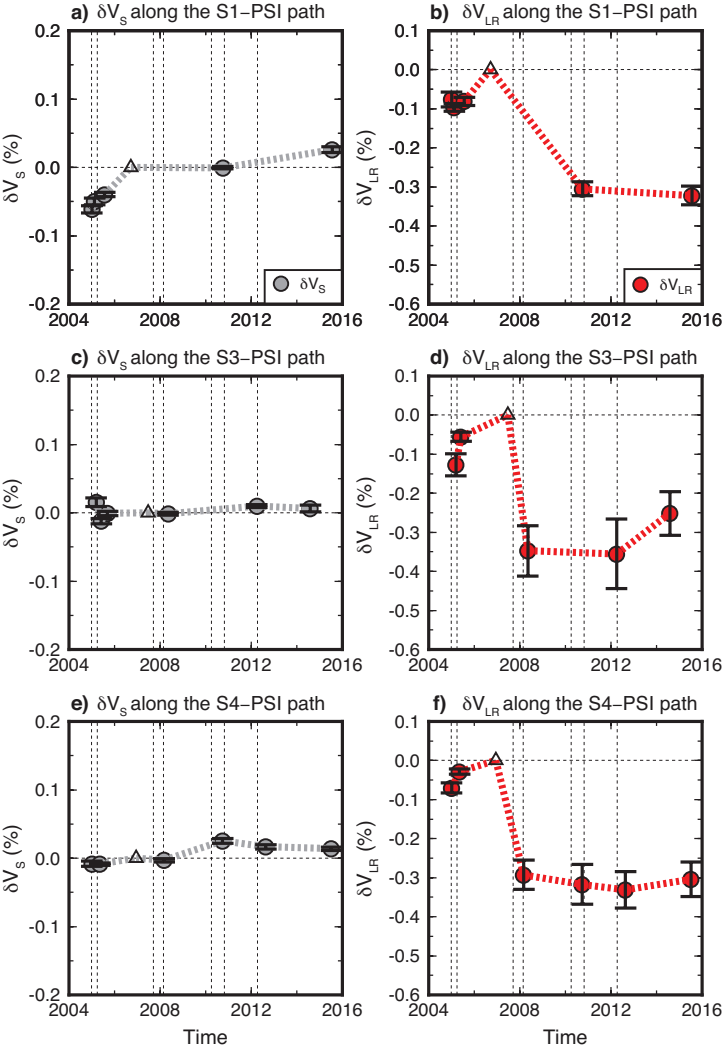
a) δV_S along the S1–PSI path
b) δV_LR along the S1–PSI path
c) δV_S along the S3–PSI path
d) δV_LR along the S3–PSI path
e) δV_S along the S4–PSI path
f) δV_LR along the S4–PSI path
δV_S (%)
δV_LR (%)
δV_S
δV_LR
0.2
0.1
0.0
-0.1
-0.2
-0.3
-0.4
-0.5
-0.6
2004
2008
2012
2016
Time

Figure 8.

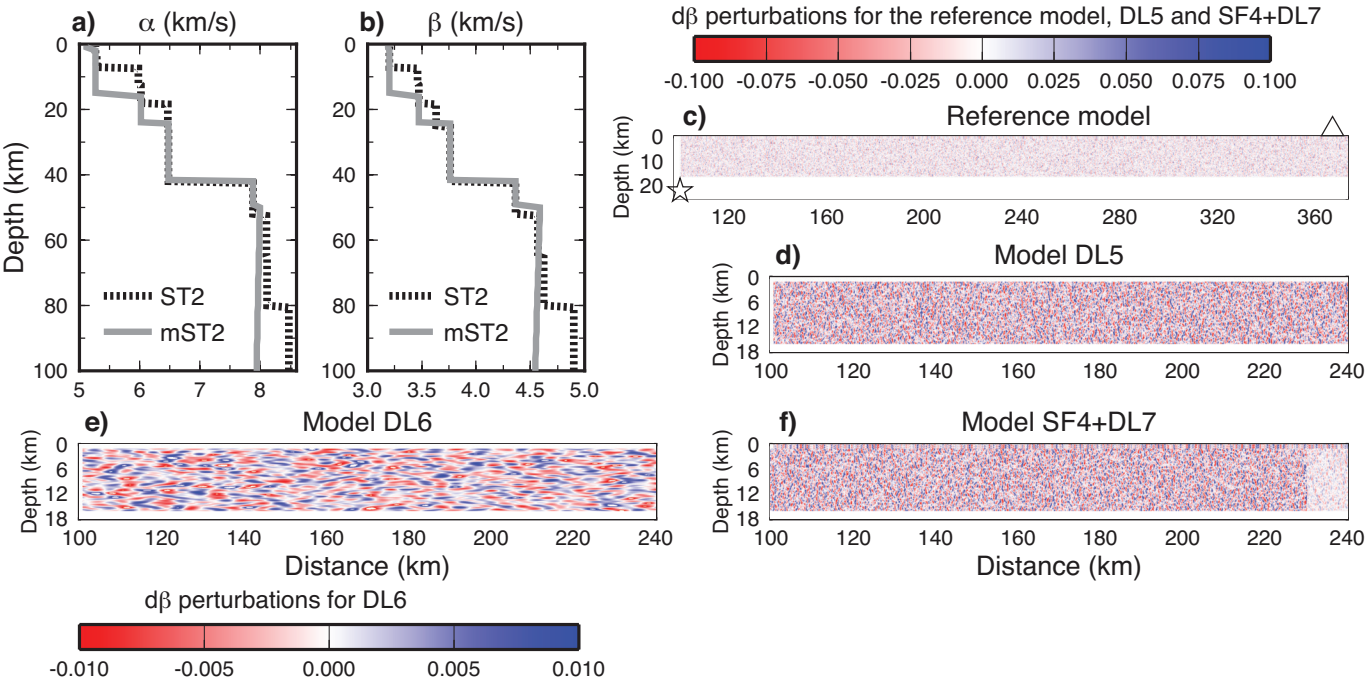
a)
α (km/s)
b)
β (km/s)
Depth (km)
ST2
mST2
dβ perturbations for the reference model, DL5 and SF4+DL7
-0.100 -0.075 -0.050 -0.025 0.000 0.025 0.050 0.075 0.100
c)
Reference model
d)
Model DL5
e)
Model DL6
f)
Model SF4+DL7
Distance (km)
dβ perturbations for DL6
-0.010 -0.005 0.000 0.005 0.010

Figure 9.

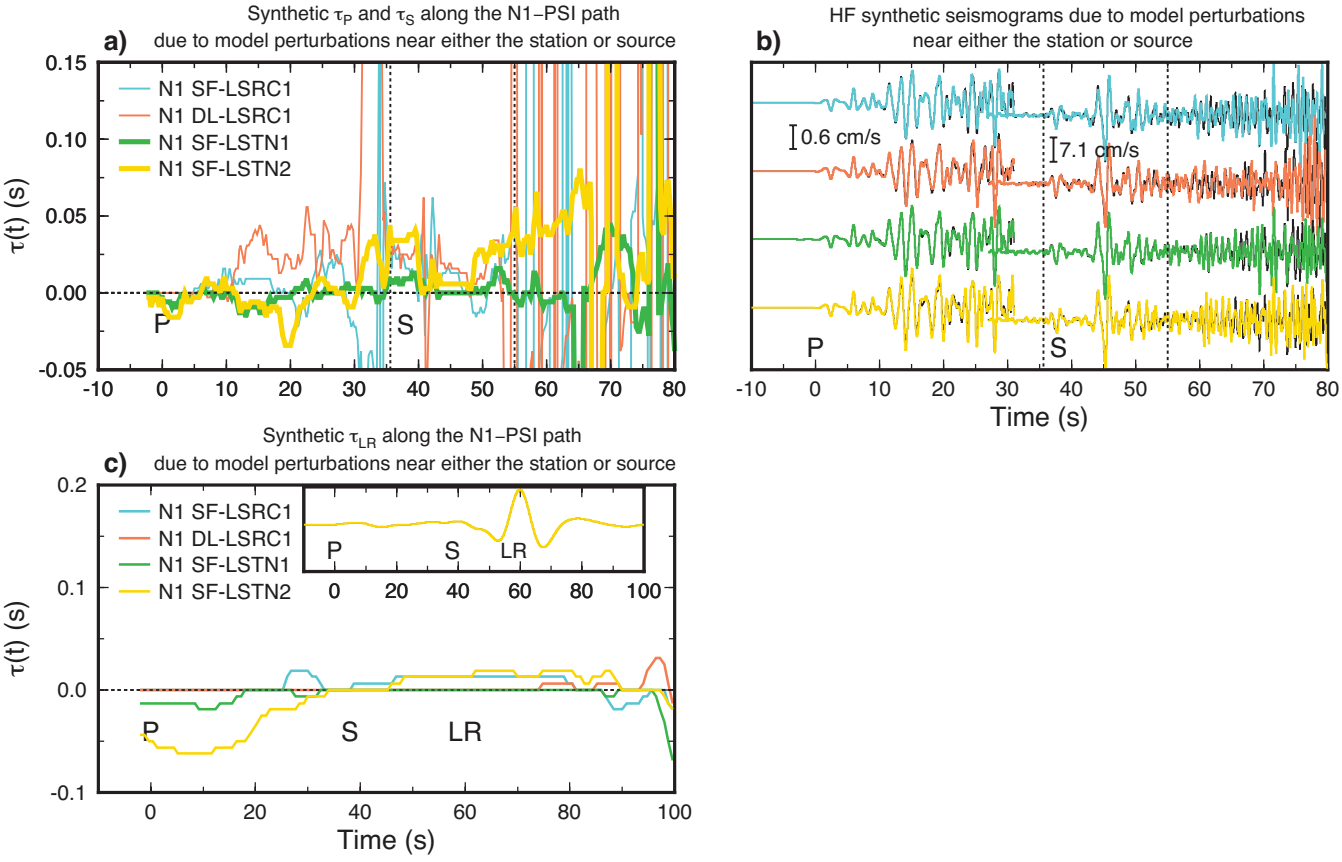
a)
Synthetic τ_P and τ_S along the N1–PSI path
due to model perturbations near either the station or source
N1 SF-LSRC1
N1 DL-LSRC1
N1 SF-LSTN1
N1 SF-LSTN2
P
S
τ(t) (s)
b)
HF synthetic seismograms due to model perturbations
near either the station or source
0.6 cm/s
7.1 cm/s
P
S
Time (s)
c)
Synthetic τ_{LR} along the N1–PSI path
due to model perturbations near either the station or source
N1 SF-LSRC1
N1 DL-LSRC1
N1 SF-LSTN1
N1 SF-LSTN2
P
S
LR
τ(t) (s)
Time (s)

Figure 10.

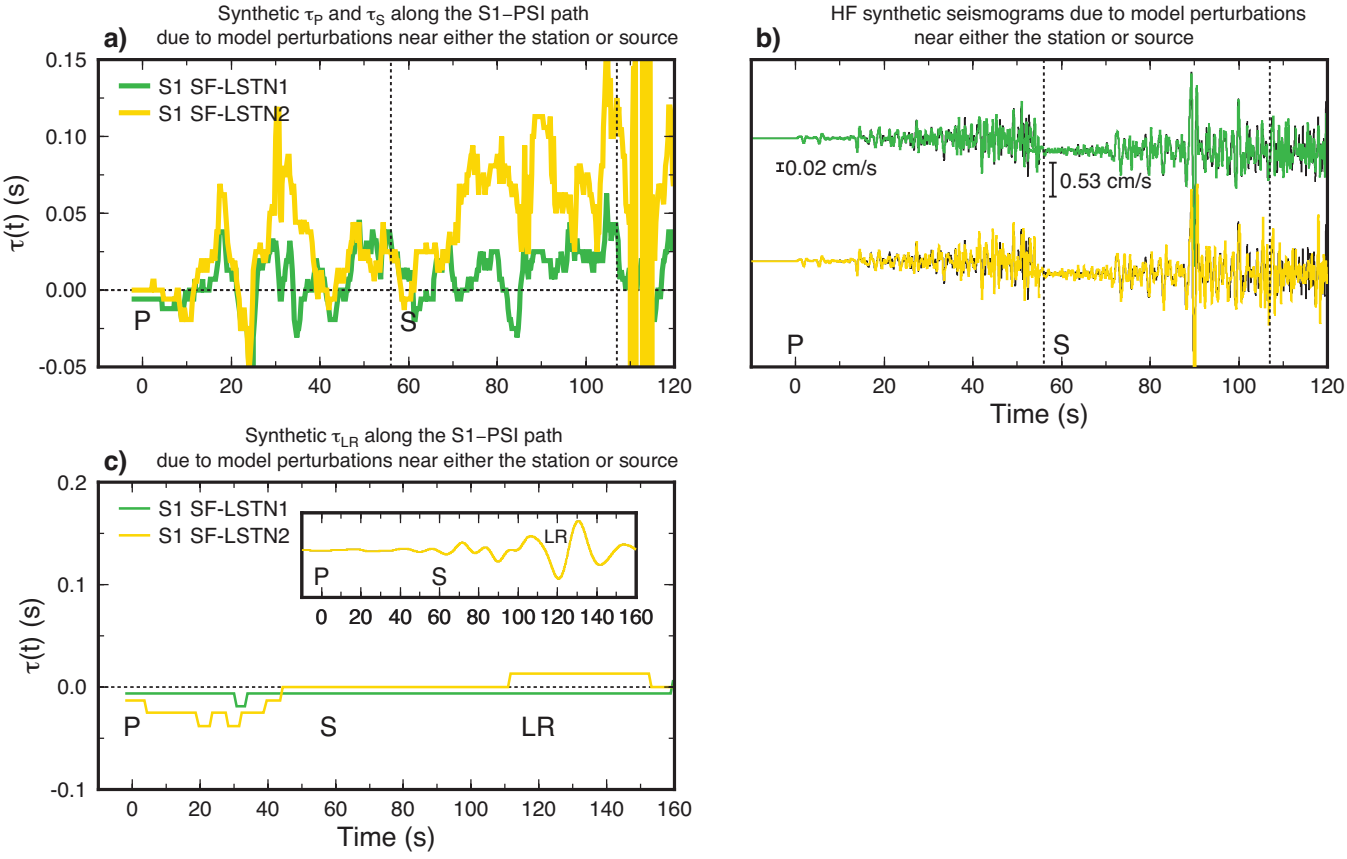
a)
Synthetic τ_P and τ_S along the S1–PSI path
due to model perturbations near either the station or source
S1 SF-LSTN1
S1 SF-LSTN2
τ(t) (s)
P
S
b)
HF synthetic seismograms due to model perturbations
near either the station or source
0.02 cm/s
0.53 cm/s
P
S
Time (s)
c)
Synthetic τ_{LR} along the S1–PSI path
due to model perturbations near either the station or source
S1 SF-LSTN1
S1 SF-LSTN2
LR
τ(t) (s)
P
S
LR
Time (s)

Figure 11.

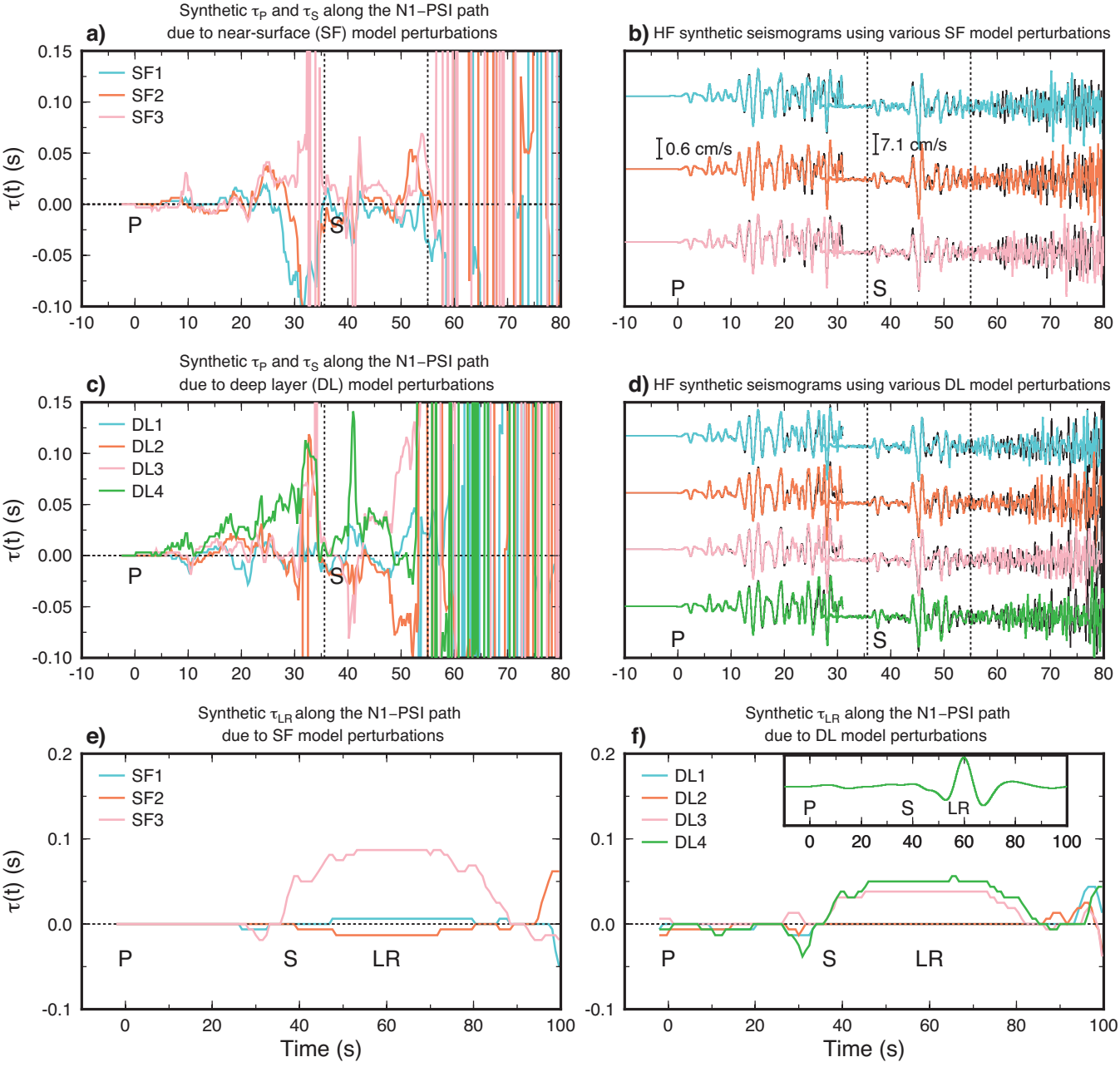
a)
Synthetic τ_P and τ_S along the N1–PSI path
due to near-surface (SF) model perturbations
SF1
SF2
SF3
P
S
τ(t) (s)
b) HF synthetic seismograms using various SF model perturbations
0.6 cm/s
7.1 cm/s
P
S
c)
Synthetic τ_P and τ_S along the N1–PSI path
due to deep layer (DL) model perturbations
DL1
DL2
DL3
DL4
P
S
τ(t) (s)
d) HF synthetic seismograms using various DL model perturbations
P
S
e)
Synthetic τ_{LR} along the N1–PSI path
due to SF model perturbations
SF1
SF2
SF3
P
S
LR
τ(t) (s)
Time (s)
f)
Synthetic τ_{LR} along the N1–PSI path
due to DL model perturbations
DL1
DL2
DL3
DL4
P
S
LR
P
S
LR
Time (s)

Figure 12.

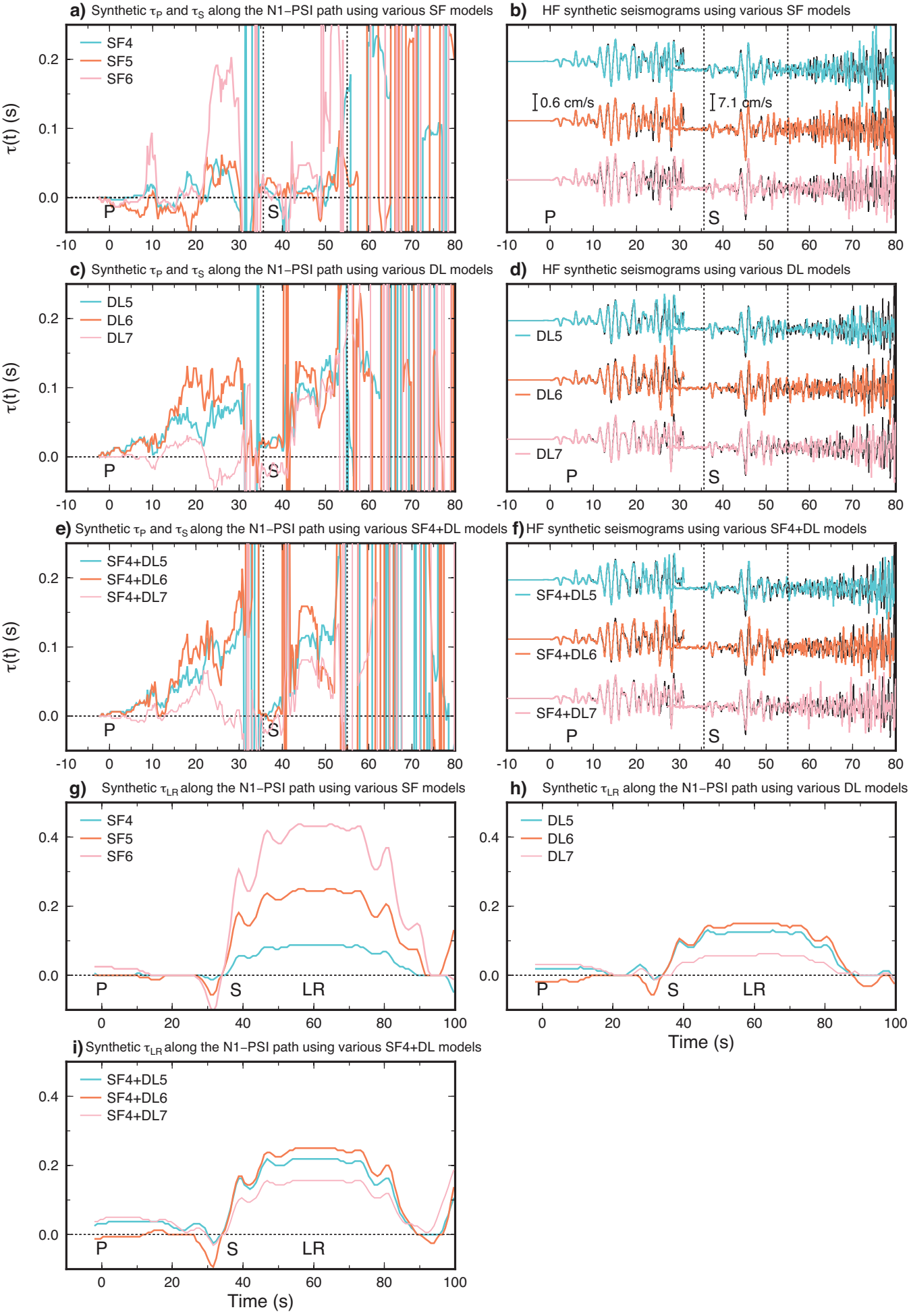
a) Synthetic τP and τS along the N1–PSI path using various SF models
SF4
SF5
SF6
τ(t) (s)
P
S
b) HF synthetic seismograms using various SF models
0.6 cm/s
7.1 cm/s
c) Synthetic τP and τS along the N1–PSI path using various DL models
DL5
DL6
DL7
d) HF synthetic seismograms using various DL models
e) Synthetic τP and τS along the N1–PSI path using various SF4+DL models
SF4+DL5
SF4+DL6
SF4+DL7
f) HF synthetic seismograms using various SF4+DL models
g) Synthetic τLR along the N1–PSI path using various SF models
LR
h) Synthetic τLR along the N1–PSI path using various DL models
Time (s)
i) Synthetic τLR along the N1–PSI path using various SF4+DL models

Figure 13.

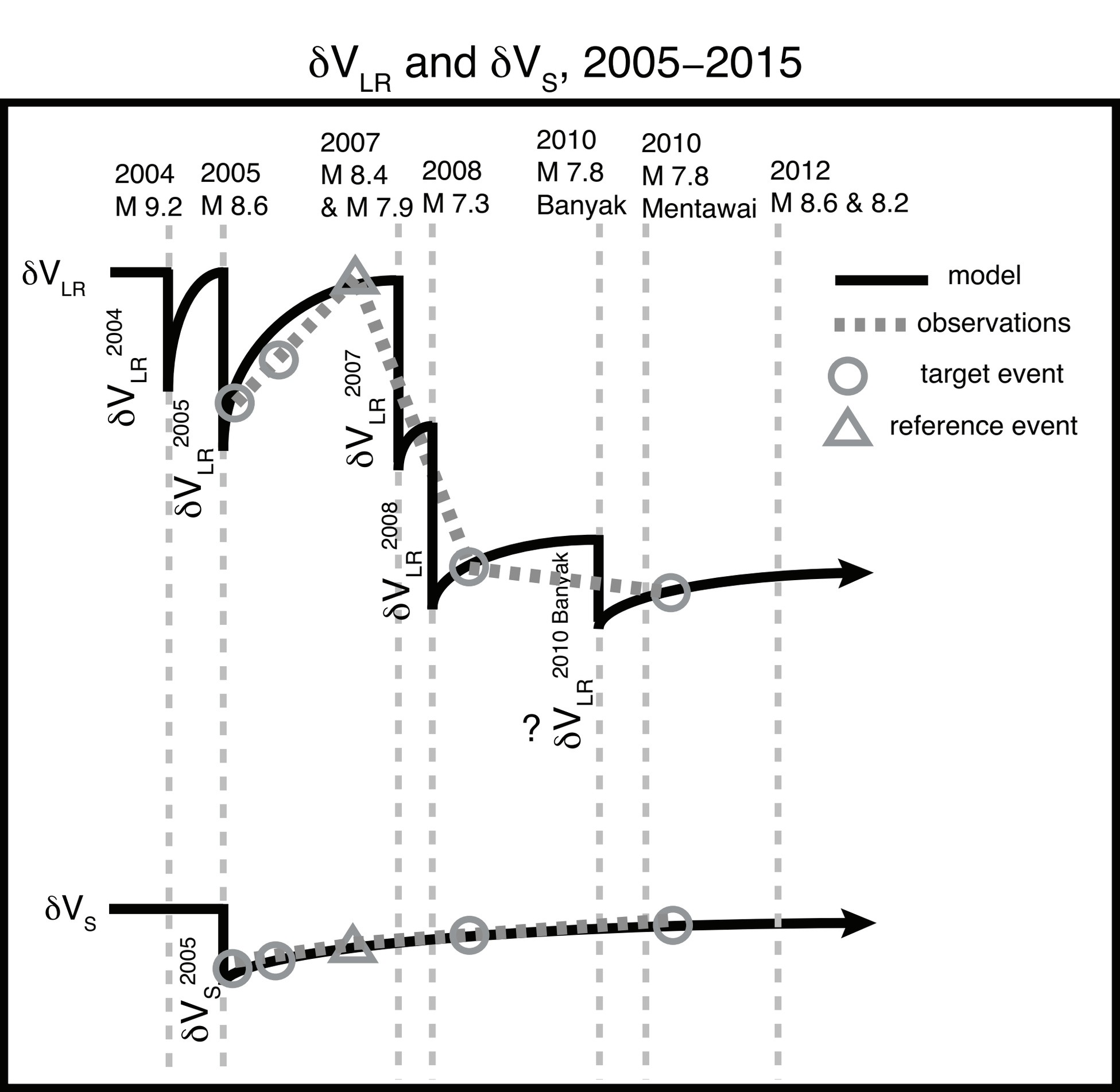
δV_LR and δV_S, 2005–2015
2004
M 9.2
2005
M 8.6
2007
M 8.4
& M 7.9
2008
M 7.3
2010
M 7.8
Banyak
2010
M 7.8
Mentawai
2012
M 8.6 & 8.2
δV_LR
δV_LR 2004
δV_LR 2005
δV_LR 2007
δV_LR 2008
δV_LR 2010 Banyak
?
model
observations
target event
reference event
δV_S
δV_S 2005